SPATIAL ORGANIZATION OF SODIUM CALCIUM EXCHANGER AND CAVEOLIN-3 IN DEVELOPING MAMMALIAN VENTRICULAR CARDIOMYOCYTES

by

HSIAO-YU HUNG

B.Sc. (Honours), Simon Fraser University, 2004

A THESIS SUBMITTED IN PARTIAL FULFILLMENT OF

THE REQUIREMENTS FOR THE DEGREE OF

MASTER OF SCIENCE

in

THE FACULTY OF GRADUATE STUDIES

(Pathology)

THE UNIVERSITY OF BRITISH COLUMBIA

(Vancouver)

April 2008

ABSTRACT

In adult cardiomyocytes, the established mechanism of excitation-contraction coupling is calcium-induced calcium release (CICR) mediated by L-type Ca^{2+} channels ($Ca_v1.2$). Briefly, membrane depolarization opens voltage-gated $Ca_v1.2$ to allow for the influx of extracellular Ca^{2+} into the cytosol. This small sarcolemmal (SL) Ca^{2+} influx is necessary for triggering a larger release of Ca^{2+} from the intracellular Ca^{2+} storage site, the sarcoplasmic reticulum (SR), through the SR Ca^{2+} release channel also known as the ryanodine receptor (RyR). RyR-mediated release of SR Ca^{2+} effectively raises the cytosolic free Ca^{2+} concentration, allowing for Ca^{2+} binding to troponin C on the troponin-tropomysin complex, leading to cross-bridge formation and cell contraction.

However, previous functional data suggests an additional CICR modality involving reverse mode Na^{+}-Ca^{2+} exchanger (NCX) activity also exists in neonate cardiomyocytes. To further our understanding of how CICR changes occur during development, we investigated the spatial arrangement of caveolin-3 (cav-3), the principle structural protein of small membrane invaginations named caveolae, and NCX in developing rabbit ventricular myocytes. Using traditional as well as novel image processing and analysis techniques, both qualitative and quantitative findings firmly establish the highly robust and organized nature of NCX and cav-3 distributions during development.

Specifically, our results show that NCX and cav-3 are distributed on the peripheral membrane as discrete clusters and are not highly colocalized throughout development. 3D distance analysis revealed that NCX and cav-3 clusters are organized with a distinct longitudinal and transverse periodicity of 1-1.5 μm and that NCX and cav-3 cluster have a pronounced tendency to be mutually exclusive on the cell periphery. Although these

findings do not support the original hypothesis that caveolae is the structuring element for a restricted microdomain facilitating NCX-CICR, our results cannot rule out the existence of such microdomain organized by other anchoring proteins. The developmentally stable distributions of NCX and cav-3 imply that the observed developmental CICR changes are achieved by the spatial re-organization of other protein partners of NCX or non-spatial modifications. In addition, the newly developed image processing and analysis techniques can have wide applicability to the investigations on the spatial distribution of other proteins and cellular structures.

TABLE OF CONTENTS

LIST OF FIGURES

LIST OF ABBREVIATIONS

$Ca_v1.2$	cardiac L-type Ca^{2+} channel
cav-1	caveolin-1
cav-2	caveolin-2
cav-3	caveolin-3
CICR	calcium-induced-calcium release
co-IP	co-immunoprecipitation
CRU	Ca^{2+} release unit
DHP	dihydropyridine
DHPR	dihydropyridine receptor
eNOS	endothelial nitric oxide synthase
ER	endoplasmic reticulum
E-C coupling	excitation-contraction coupling
GPCR	G-protein-coupled receptors
GPI	glycosylphophatidylinositol
I_{Ca}	L-type Ca^{2+} current
I_{NCX}	NCX current
LSCM	laser scanning confocal microscopy
L-type-CICR	L-type Ca^{2+} channel-mediated CICR
MLE	maximum likelihood estimation
$Na_v1.5$	cardiac Na^+ channel α subunit
NCX	sodium calcium exchanger

NCX-CICR	NCX-mediated CICR
PBS	phosphate-buffered saline
PLB	phospholamban
PMT	photomultiplier tube
RPM	revolutions per minute
RyR	ryanodine receptor
SERCA2a	cardiac sarcoplasmic reticulum Ca^{2+} ATPase
SOC	store operated channels
SL	sarcolemma
SR	sarcoplasmic reticulum
TRPC	transient receptor potential canonical channels
T-tubules	transverse tubules

ACKNOWLEDGEMENTS

The past three years have been the most challenging years of my life yet. I have grown much as an individual during this period, particularly towards the end of this project. However, this endeavour would not have been completed without the help of many people who have generously devoted their resources to me. First and foremost, I would like to begin by thanking my senior supervisor, Dr. Glen Tibbits, for his mentorship, guidance, and support, both academically and personally. Dr. Tibbits has shown me more patience than anyone I have ever known and amongst many things, has taught me the true meaning of dedication.

I am grateful to my supervisory committee members, Dr. Bruce Verchere, Dr. Bruce McManus, and Dr. Edwin Moore for their time and attention. I thank other members of CMRL for making the lab a pleasant and fun place to be. In particular, I thank Haruyo Kashihara for all her help and encouragements. A special thank you goes to my fellow colleague Eric Lin, without whom this project would not have been completed. In addition to his intellectual contribution to this project, Eric has endured many hours of emotional assault from me and has taught me many life lessons. I would also like to thank my parents, Kun-Nan Hung and Mei-Kuei Yu, for their unconditional love and financial support through these years.

Lastly, I would like to express my gratitude to the scientific funding agencies for supporting this project. In particular, Canadian Institutes of Health Research has provided the majority of the operating funds and the University of British Columbia, Department of Pathology offered a graduate studentship to me.

CO-AUTHORSHIP STATEMENT

This project was completed chiefly by the joint efforts of Mr. Eric Lin, Dr. Glen Tibbits and me. I was directly responsible for the formulation of the experimental design, the execution of the actual experiments, and the preparation of the resulting manuscript. Ms. Haruyo Kashihara offered her technical expertise to this project by performing the cell isolation procedures. Mr. Eric Lin was responsible for the majority of the data analysis and was a first co-author on the manuscript. Dr. Glen Tibbits provided much guidance, support, and input on the data analysis, manuscript preparation, and overall project planning and implementation.

CHAPTER I: INTRODUCTION

1.1 Research Problem

During mammalian heart development, both cell morphology and excitation contraction (E-C) coupling mechanisms undergo significant changes (1). These phenotypic differences result in differential responses of adult and pediatric patients to physiological, pathological and surgical perturbations. Since past investigations have mainly focused on the adult cardiac systems, most of the current pharmacological and surgical treatments were developed based on our understanding of the adult systems. Thus some of these treatments are not always appropriate for pediatric patients. For example, the discharge mortality rate of pediatric open heart surgery patients has historically been higher than that of adult patients. Recent efforts of researchers and clinicians attempting to develop protocols more specific to pediatric patients have lowered the mortality rate of pediatric cardiac surgery to below 5% in most centres (2,3) yet such rates still remain considerably higher than that reported for adults at 3% (4). More detailed analysis showed that even within the pediatric group, young age is an important risk factor for mortality (2). These problems present an imminent need to improve our understanding of the neonatal heart systems and the ontogeny of such systems.

1.2 Adult Heart

1.2.1 E-C Coupling to CICR

E-C coupling is the process that couples membrane depolarization to muscle contractions. As Ca^{2+} is the main mediator of this process, cytosolic levels of Ca^{2+} are always tightly regulated by many different mechanisms. In the adult mammalian heart, calcium-induced calcium release (CICR) is a widely accepted mechanism of E-C coupling. Since the general acceptance of the CICR hypothesis based on experiments published in 1983 by Fabiato (5), many subsequent studies have revealed numerous proteins involved in this pathway and a general consensus is compiled.

In CICR, membrane depolarization opens L-type Ca^{2+} channels ($Ca_v1.2$) to allow for influx of extracellular Ca^{2+} into the cytosol. This small sarcolemmal (SL) Ca^{2+} influx is necessary in triggering a larger release of Ca^{2+} from the sarcoplasmic reticulum (SR) through the SR Ca^{2+} release channel, ryanodine receptor (RyR). RyR-mediated release of SR Ca^{2+} effectively raises the intracellular free Ca^{2+} concentration ($[Ca^{2+}]_i$). The free Ca^{2+} then binds to the troponin C protein on the troponin-tropomysin complex, allowing for cross-bridge formation, and initiates cell contraction (6).

In the resting (or diastolic) state, cytosolic bulk phase $[Ca^{2+}]_i$ is ~100 nM. During an action potential, the bulk phase $[Ca^{2+}]_i$ can be transiently increased to almost 1 μM. Thus to maintain Ca^{2+} homeostasis, an equal amount of Ca^{2+} extrusion to Ca^{2+} entry must occur with each contraction. As such, to achieve relaxation, cytosolic Ca^{2+} is lowered to resting levels, mainly by Ca^{2+} reuptake into the SR via SR Ca^{2+} ATPase (SERCA2A) and extrusion into the

extracellular space by forward mode sodium-calcium exchanger (NCX) activity (6) (see Figure 1).

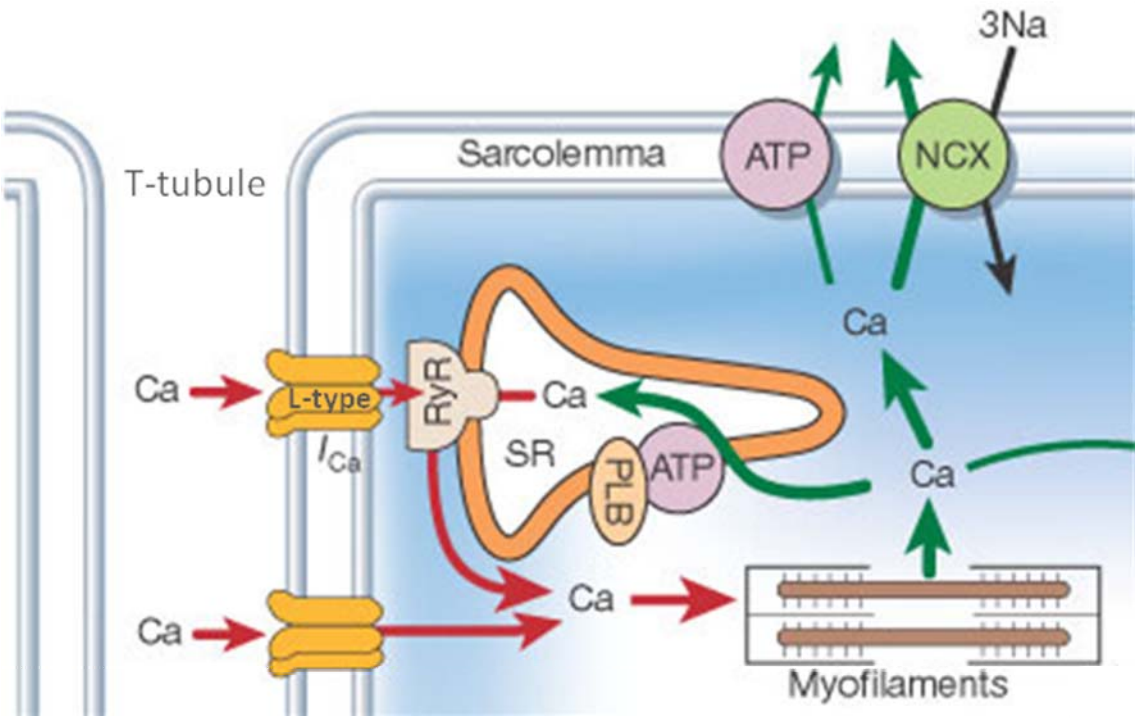

Figure 1: Excitation-contraction coupling in adult mammalian heart.
Schematic representation of E-C coupling in adult ventricular myocyte. Adapted by permission from Macmillan Publishers Ltd. (7). Membrane depolarization opens L-type Ca^{2+} channels on the T-tubular membrane to allow for a small extracellular influx of Ca^{2+}. This SL Ca^{2+} influx triggers SR Ca^{2+} release via RyR, effectively raising the cytosolic free Ca^{2+}, allowing for Ca^{2+} binding to the myofilaments thus leading to cell contraction. Cell relaxation is achieved by Ca^{2+} extrusion via forward mode NCX activity, SL Ca^{2+} ATPase, and reuptake of Ca^{2+} into the SR by SERCA. SERCA activity is regulated by its binding to phospholamban (PLB). Dephosphorylated PLB inhibits SERCA activity, thereby decreases SR Ca^{2+} reuptake. Upon PLB phosphorylation mediated through beta-adrenergic stimulation, the inhibitory effect of PLB on SERCA is relieved.

CICR has two special properties: the graded response and high gain. The graded response refers to the fact that the level of SR Ca^{2+} release is a function of the trigger Ca^{2+}

influx amplitude and rate. This implies that the magnitude of contraction can be modulated by supplying differing levels of the trigger Ca^{2+} current. The gain of CICR is a measure used to describe the relationship between the magnitude of the trigger Ca^{2+} current and the SR Ca^{2+} release. It is the amplification factor of CICR calculated as the SR Ca^{2+} release divided by the Ca^{2+} trigger signal that produces it. CICR gain varies in different species and methods of the measurement. For example, in adult rat ventricle, a gain of 16 at 0 mV membrane potential has been reported (8); in adult rabbits, a gain of 3 - 8 has been reported (9).

Since the initial discovery of CICR as the primary E-C coupling mechanism in ventricular myocytes, there have been many studies trying to model the details of cardiac CICR. In these attempts, several models have been proposed including: 1) common pool models, 2) local control models, and 3) ad hoc models. The ad hoc approach, originally proposed by Luo and Rudy (10), correctly predicts the gain of E-C coupling, but overlooks certain spatial details of Ca^{2+} handling proteins. In common pool models, all RyR channels sense a common cytosolic pool of Ca^{2+} entered via $Ca_v1.2$, resulting in an "all or nothing" response (all RyR channels release or none releases) (11-13). However, this model is inconsistent with experimental observations in which the induced Ca^{2+} release is approximately proportional to the trigger current (14-16). To circumvent this problem, the local control model was developed (8,17,18). Local control theory asserts that RyR are sensitive to local rather than global Ca^{2+} levels such that variations in $[Ca^{2+}]_i$ will allow for activation of some RyR channels but not all. Each opening event is detected as a spontaneous local increase in $[Ca^{2+}]_i$ defined as a calcium spark. Calcium sparks are regarded as the elementary release units of Ca^{2+} in CICR from Ca^{2+} release units (CRU) each consisting of at least the SR Ca^{2+} release channel, RyR, and the sarcolemmal Ca^{2+} influx

channel, namely the $Ca_v1.2$ in adult ventricular myocytes. The total rise in $[Ca^{2+}]_i$ is then the summation of all calcium sparks. The existence of individually activated CRUs forms the basis the local control theory.

1.2.2 Protein Localization in Adult Heart

In mature ventricular myocytes, NCX1.1, the cardiac specific form of NCX, appears to be localized primarily in the T-tubules. Both immunofluorescence confocal images and immunogold electron micrographs indicate that the majority of NCX1.1 is located in both the longitudinal and transverse elements of the T-tubules and the intercalated discs. Meanwhile, some NCX1.1 are also observed on the peripheral SL (19-21).

In adult rat ventricular myocytes, Na^+ channels are also distributed in both transverse and longitudinal components of the T-tubules, but in areas separate from NCX since the two proteins do not colocalize (20). In addition to the classically recognized cardiac α subunit isoform, $Na_v1.5$, which is found primarily in the intercalated disks, an unexpected presence and functional roles for brain-type α subunit isoforms were found in mouse ventricular myocytes (22,23). Maier et al. established that $Na_v1.1$, $Na_v1.3$, and $Na_v1.6$ are preferentially localized to the T-tubules. Not only do different α subunits exhibit differential cellular spatial specificities, different regulatory β subunits also occupy different cellular locations. The β_2 subunit is found together with $Na_v1.5$ in the intercalated disks whereas β_1 and β_3 are localized to the T-tubules (22).

In contrast to NCX and Na^+ channel distributions, $Ca_v1.2$ are distributed only along the transverse elements of T-tubule membranes and therefore are found solely at the Z-lines, occurring with a ~2 μm periodicity. Both electron microscopy and fluorescent microscopy techniques showed that RyR exhibits a similar pattern of distribution, located largely on the

SR membrane adjacent to T-tubules, thus appearing predominantly along the Z-lines (20,24-26).

Given the similarities in the distribution patterns, it is not surprising to find these two proteins closely associated. Double immunolabeling experiments showed a high degree of colocalization between $Ca_v1.2$ and RyR at the dyads in adult rabbit ventricular myocytes (24). Subsequently, Scriven et al. confirmed this result in adult rat ventricular myocytes. In addition, they also demonstrated the absence of NCX and Na^+ channels in these dyads. Dyads, a cardiac equivalent of triads in skeletal muscles, are specialized junctions in cardiac muscles formed between the T-tubular membrane and a closely apposed SR, thus serving as the primary sites of CICR. These findings provide a structural explanation for the observed L-type-mediated CICR in adult ventricular myocytes.

1.2.3 NCX Structure and Function

NCX1.1 has been modeled to contain 9 transmembrane segments with a large intracellular loop between transmembrane segments 5 and 6. The large intracellular loop houses an exchanger inhibitory peptide (XIP) site involved in Na^+ dependent inactivation, a regulatory Ca^{2+} binding site, and a tissue specific alternative splice site. The protein also contains two reentrant loops connecting transmembrane segments 2 and 3 as well as transmembrane segments 7 and 8. These reentrant loops contain two α repeats that are important in the actual ion binding and translocation process (27-29) (see Figure 2).

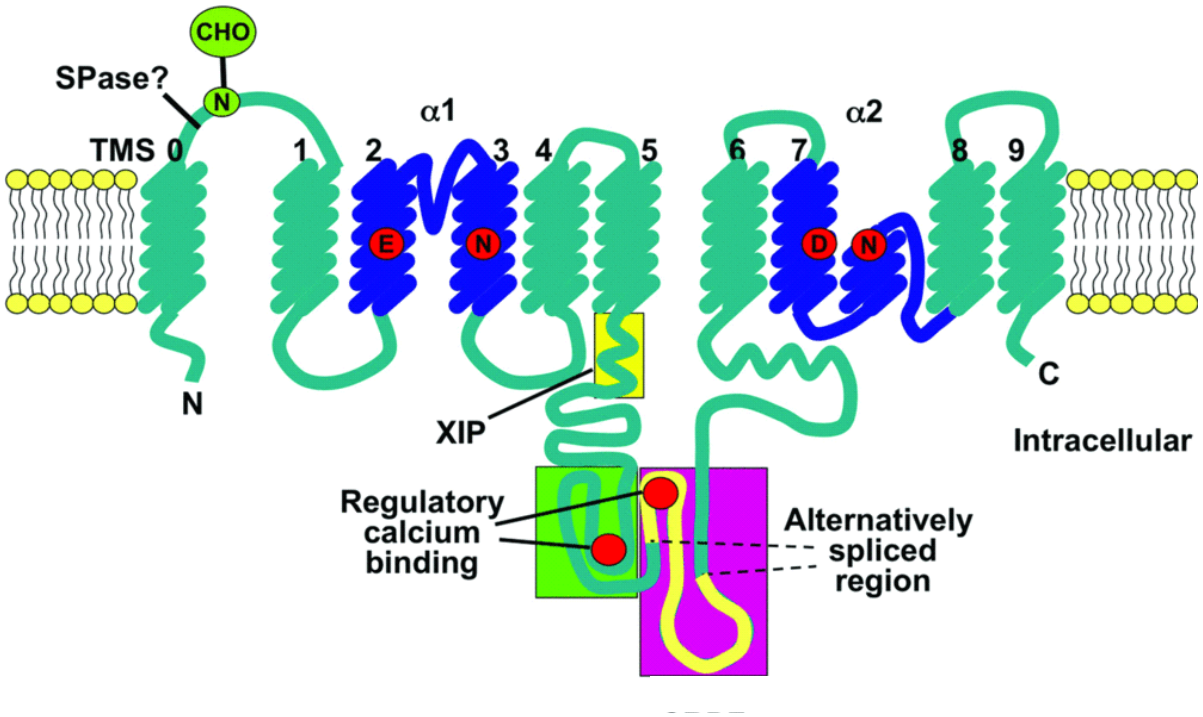

Figure 2: Putative NCX topology model.
NCX topology model proposed by Lytton (30). NCX1.1 has been modeled to contain 9 transmembrane segments with a large intracellular loop between transmembrane segments 5 and 6. The large intracellular loop houses an exchanger inhibitory peptide (XIP) site involved in Na^+ dependent inactivation, a regulatory Ca^{2+} binding site, and a tissue specific alternative splice site. Transmembrane segment 0 is a cleaved signal peptide with the putative cleavage site shown as SPase?. The protein also contains two re-entrant loops connecting transmembrane segments 2 and 3 as well as transmembrane segments 7 and 8. Areas in dark blue represent the two α repeats that are important in the actual ion binding and translocation process. In addition, the first extracellular segment, occurring between transmembrane segments 0 and 1, is glycosylated.

Long before the protein topology of NCX was proposed, the stoichiometry of NCX had been determined as 3 Na^+ ions for exchange of every 1 Ca^{2+} ion across the SL (31). Since NCX is a bidirectional exchanger, the direction of ion movement is determined by Na^+ and Ca^{2+} gradient and membrane potential (32), in particular by local [Na^+] and [Ca^{2+}] in the subsarcolemmal microdomain region where the reversal potential of NCX is calculated by the following equation: $E_{NCX} = 3E_{Na} - 2E_{Ca}$. Under normal physiological conditions in adult ventricular cells, NCX reversal potential is ~40 mV where as ventricular myocyte membrane potential is -80 mV, thus NCX is believed to be operating in forward mode, extruding Ca^{2+} from the cell. Under certain conditions, NCX has also been proposed to operate in reverse mode, bringing Ca^{2+} into the cytosol. Bers (33) has suggested that a local change in [Na^+] as small as 3 mM can produce a significant increase of Ca^{2+} influx via NCX (33). Therefore, given the wide range of $[Na^+]_i$ found in different species and under different experimental conditions (34-36), the direction of NCX operation and by extension the role of NCX in E-C coupling will likely differ.

Considering the important role NCX plays in cardiac cell Ca^{2+} efflux, it was surprising to see cardiac-specific NCX knockout mice viable to adulthood and appear relatively healthy on an organismic level. Closer examination on the cellular level identified two adaptations of E-C coupling in these cardiac cells: 1) a reduction of current via $Ca_v1.2$ (I_{Ca}) coupled with an increase in E-C coupling gain; 2) a shortening of the action potential (37). Both of these observations are interpreted as adaptive mechanisms that maintain Ca^{2+} homeostasis by limiting Ca^{2+} influx while preserving contractility.

In addition to the adaptive responses, other factors may also explain the relatively normal phenotype of cardiac-specific NCX knockout mice. Previously, a global knockout of

NCX was generated and proved to be lethal in a murine model. The cardiac-specific murine NCX knockout model discussed here was generated using the cre/lox system. Thus, incomplete penetrance of the tissue-specific knockout may partially explain the relatively normal phenotype in these cells. In addition, it has long been noted that differences exist in the action potential profiles as well as Ca^{2+} handling mechanisms even amongst mammalian species. For example, the NCX contribution to Ca^{2+} homeostasis is relatively minor in murine hearts when compared to other mammalian species such as human or rabbit. It is estimated that the contribution of NCX to relaxation on a beat to beat basis is ~25% in rabbits, but only 10% in mice and rat ventricular myocytes (6). In fact, Sarai et al. (38) has determined that models of mammalian species showing high square plateau action potential, including guinea pig, human, and rabbit ventricular myocytes, are much less resistance to NCX knockout than the mouse model. Thus, one must be careful in extending the interpretations of knockout mice data to other model systems.

1.3 Developing Heart

1.3.1 Myocyte Structure

During myocyte development, the cell undergoes many structural changes including cell size, cell shape, total cell membrane capacitance, and other ultrastructural changes. For example, rabbit ventricular myocyte cell size increases in both length and diameter from approximately 50 and 5 μm in 3 day old cells to greater than 100 and 20 μm in 56 day old cells. In these cells, the cell shape also changes from a smooth cylindrical shape with tapered ends to a more rectangular shape with well-organized striations (39-43).

Perhaps one of the most notable ultrastructural differences between neonatal and mature ventricular myocyte is the development of transverse tubules (T-tubules). T-tubules are a unique feature in striated muscle cells that allow for the rapid propagation of depolarization into the interior of the cell, leading to synchronous Ca^{2+} release. As mentioned in section 1.2.2, the T-tubular network has two components: a transverse element and a longitudinal element. Recent studies have reported that the transverse component of T-tubules, occurring at the Z-lines with an interval of around 2 μm, make up 60% of T-tubular volume. The remaining 40% of T-tubules occurs between the Z-lines as longitudinal extensions running parallel to the long axis of the cell (44). Since many proteins involved in E-C coupling appear to be concentrated at the T-tubules, they have been suggested as the main site of E-C coupling (45). As such, the development of T-tubule also suggests that E-C coupling mechanisms and organizations may also undergo drastic developmental changes.

On the other hand, early electron micrographs suggest that SR appear relatively sparser in neonatal ventricular myocytes compared to adult myocytes (46,47). This

observation led to the speculation that CICR may not be the major E-C coupling mechanism in the neonatal heart. However, it has also been reported that surface dyads are evident even at very early stages of development (46,48) and the density of these dyads has already reached adult values at one day after birth (46). Thus, morphological evidence alone may not appropriately reveal developmental changes in SR involvement during E-C coupling.

1.3.2 Protein Expression Changes During Development

Nowycky et al. (49) first developed the classification of voltage gated Ca^{2+} channels as L, T and N types that has since been generally adopted. L-type Ca^{2+} channels are characterized by a **l**arge conductance, **l**ong lasting openings, activation at **l**arger depolarizations, and sensitivity to dihydropyridines (DHP). Consequently, L-type Ca^{2+} channels are also called dihydropyridine receptors (DHPR). T-type Ca^{2+} channels are characterized by a **t**iny conductance, **t**ransient openings, an activation at more negative membrane potential, and insensitivity to DHP. N-type Ca^{2+} channels are name as such because they are predominantly found in **n**eurons and exhibit intermediate conductance and voltage dependence properties. Subsequently, P-type (Purkinje cells), Q-type (granular cells), and R-type (toxin-resistant) Ca^{2+} channels were also distinguished based on their tissue specificities or toxin sensitivities (50).

In ventricular myocytes, L-type Ca^{2+} channels are the predominant isoform expressed. L-type Ca^{2+} channels are made up of several subunits: α_1, α_2, β, and δ. The α_1 subunit of the L-type Ca^{2+} channel serves as the main subunit forming the pore of the channel, voltage sensor, and the selectivity filter. It is also the subunit containing the binding sites for several classes of Ca^{2+} antagonists including the DHP. The α_2, β and δ subunits of the L-type Ca^{2+} channel, while not essential for channel function, have important regulatory effects (6).

In 2000, Ertel et al. (51) proposed a more uniform nomenclature for the α_1 subunits which is now commonly used. In this new nomenclature, the 4 classes of L-type Ca^{2+} channel α_1 subunits, α_{1S}, α_{1C}, α_{1D} and α_{1F}, are re-named as $Ca_v1.1$, $Ca_v1.2$, $Ca_v1.3$, and $Ca_v1.4$ respectively. To date, alternative splice variants of $Ca_v1.1$, $Ca_v1.2$, and $Ca_v1.3$ have all been identified (50). However, the cardiac specific isoform, $Ca_v1.2$, is the only one showing developmentally regulated alternative splicing. In 2006, Huang et al. (52) examined the existence of different splice variants in the rabbit heart and found two different developmental splice variants of $Ca_v1.2$, IVS3A and IVS3B. These two splice variants differ in the fourth motif of the third transmembrane segment. The authors found IVS3A to be the dominant isoform at early developmental stages; but as cells develop, IVS3A was gradually replaced by IVS3B. This switch in $Ca_V1.2$ isoform expression was not associated with any obvious changes in activation kinetics, DHP binding properties, or the current-voltage relationship parameters. However, this differential isoform expression pattern is temporally correlated with the appearance and robustness of I_{Ca}-dependent E-C coupling (52). The authors proposed that each isoform may have distinct sub-cellular distribution thus affecting E-C coupling functions. For example, IVS3A may be preferentially expressed on the SL and IVS3B in the T-tubules.

Another E-C coupling protein exhibiting developmentally regulated isoform switching is $Na_v1.5$. Haufe et al. (53) noted that $Na_v1.5$ switches from neonate dominating form $Na_v1.5a$ to adult dominating $Na_v1.5b$. Unfortunately, the significance of this developmentally regulated Na^+ channel isoform switch remains unknown and requires further investigation.

In mammalian cells, there are also several isoforms of SERCA, each exhibiting a distinct pattern of tissue specificity (54-59). SERCA1 is expressed in fast twitch skeletal muscle, although two developmental isoforms exists. In fetal and neonatal fast twitch skeletal cells, SERCA1b is expressed; however, SERCA1a predominates in the adult. SERCA2 also generates two isoforms that differ in their C-terminal tail. SERCA2a is the muscle-specific isoform with a short amino acid tail expressed in slow twitch skeletal as well as cardiac muscles; the ubiquitous SERCA2b has extended tail residues for attachment on the SR membrane (60). Like SERCA2b, SERCA3 is also ubiquitously expressed in a variety of muscle and non-muscle tissues.

To date, SERCA2a has not been shown to exhibit developmental isoform change. But a down-regulation of SERCA2a has been observed in heart failure (61). Several studies have indicated that at birth, mRNAs and protein expression levels of SERCA2a in cardiac myocytes are approximately 50% that of adult levels. SERCA2a expression level gradually increases to adult levels by 15 day post-partum (62,63).

Other studies have also indicated that NCX mRNA and protein levels, as well as peak NCX current (I_{NCX}) change during development, ranging from 2-6 times higher at birth than adult values (64-66). This may imply that NCX may play a more important role in E-C coupling in neonatal systems.

1.3.3 CICR Changes During Development

As mentioned in the previous section (1.3.2), the developmental isoform switching of $Ca_v1.2$ has potential implications in CICR changes during development. In fact, an increasing role of $Ca_v1.2$ in E-C coupling during development is well documented (5,52,66-68), although some species dependence of this increasing role has also been noted (69-71).

In rabbit ventricular myocyte, electrophysiological data supported this notion by demonstrating the fraction of nifedipine-sensitive Ca^{2+} transient increases with age, from 20% in 3 day old myocytes to 90% in 56 day old myocytes (52). Because nifedipine is a $Ca_v1.2$ blocker, nifedipine-sensitive Ca^{2+} transient presumably represents contribution from L-type-mediated CICR (L-type-CICR) (52).

Although NCX is traditionally regarded as the prominent Ca^{2+} removal mechanism in E-C coupling, as mentioned before, NCX can also operate in reverse mode. A role for reverse mode NCX in CICR has been inferred in adult ventricular myocytes. Litwin et al., and Kohomoto et al., have demonstrated the existence of NCX-mediated CICR (NCX-CICR) in adult rabbit and guinea pig ventricular myocytes (72,73). Similarly, Nuss et al. also reported NCX-CICR in ferret ventricular myocytes although under elevated $[Na^+]_i$ conditions (35). On the other hand, Huang et al. (40) concluded that reverse mode NCX and NCX-CICR is not present in the adult rabbit myocytes since application of nifidepine completely abolishes the Ca^{2+} transient. This broad difference might be attributed to differences in experimental protocols and/or the uses of different animal models.

While the physiological significance of NCX-CICR in adult ventricular myocytes remains controversial, its role in neonatal is even less established. Initially, Haddock et al. (74) reported in 1999 that the Ca^{2+} transient triggered by the field stimulation in neonatal rabbit ventricular myocytes does not seem to involve appreciable SR Ca^{2+} release due to the relative insensitivity of contractions to ryanodine, an RyR blocker, and thapsigargin, a SERCA inhibitor. However, more recently Seki et al. demonstrated in fetal rat myocytes that Ca^{2+} transient is in fact sensitive to inhibition by thapsigargin, in both the subsarcolemmal space and the cell center (75). Functional data from our own laboratory also showed that in

neonatal rabbit ventricular myocytes, application of nifedipine does not eliminate contraction; however, the subsequent additional of KB-R 7943, a NCX inhibitor, does prevent contraction. Furthermore, the fraction of this NCX-sensitive, SR Ca^{2+} sensitive Ca^{2+} transient to total SR Ca^{2+} sensitive Ca^{2+} transient decreases significantly with age from 37% in 3 day old cells to ~ 0.5% in 56 day old cells (unpublished results).

In fact, in addition to functional evidence, spatial information from imaging studies also support the notion that NCX-CICR is more physiologically relevant in neonatal ventricular myocytes than in adult. Dan et al. (76) recently demonstrated that NCX exists as high density protein clusters even in early developmental stages and the degree of colocalization between NCX and RyR is higher in neonatal cells.

In essence, it seems at least in neonatal rabbit ventricular myocytes, there is a physiologically relevant contribution of NCX-CICR, and this contribution decreases significantly with development while the contribution of L-type-CICR increases significantly during development. Although the unitary influx rate via $Ca_v1.2$ is 100 - 1000 times greater than that via NCX (77), NCX-CICR gain is only 3 times smaller when compared to L-type-CICR gain. This could be attributed to a combination of factors, including the protein densities the spatial organization of the relevant proteins.

1.3.4 Protein Localization in Neonatal Cells

As discussed in section 1.2.2, $Ca_v1.2$ is mainly localized to the T-tubules in adult mammalian heart. Interestingly, even before the development of T-tubules, $Ca_v1.2$ is already organized as discrete clusters on the SL with a periodicity of ~2 um in register with the Z-lines (78). Thus $Ca_v1.2$ appears to be anchored to the cytoskeleton in a manner that has not

yet been determined, and such anchorage is likely important in subsequent developmental processes.

Another important molecule in E-C coupling, NCX, also undergoes extensive distribution changes during development. In neonatal cells, it has been previously reported that NCX was distributed homogeneously at the cell surface (65,67,74). However, a recent study has challenged this view by demonstrating that more than 90% of NCX found in neonatal rabbit ventricular myocytes are already organized into discrete clusters located at or near the cell surface with a periodicity of ~0.7 μm (76). The authors reported that as cells develop, NCX gradually migrates into the cell interior, with about 70% of total label residing in cell interior in adult cells. The interior NCX clusters in these cells display a periodicity near 2.0 μm, consistent with previous reports (79). Interestingly, despite the developmental change in NCX protein distribution pattern, the peripheral periodicity of NCX remains at ~0.7 μm in adult cells.

In the same study, the authors also found two major developmental differences in RyR distribution: 1) the longitudinal periodicity of RyR clusters changes from ~0.7 μm in the neonate to ~2.0 μm in adult, and 2) the ratio of peripheral to interior label changes significantly from surface dominating (60% to 40%) to interior dominating (90% to 10%) (76). As RyR is the site of intracellular Ca^{2+} release, this change in RyR distribution could be one mechanism responsible for facilitating the CICR changes observed during development.

When considering how developmental distribution changes affect function, it is important to also consider the relative spatial relationship between relevant proteins that are likely organized in the same functional unit, the CRU. Thus, several studies have

investigated the degree of colocalization between $Ca_v1.2$ and RyR, as well as between NCX and RyR. As expected, structural coupling between $Ca_v1.2$ and RyR increases significantly during development from 43% in 3 day old cells to 79% in 20 day old cells (78,80).

Conversely, the degree of colocalization between NCX and RyR exhibits a gradually decreasing trend where colocalization is highest in 3 day old rabbit ventricular myocytes at 14% and drops down to 10% in 56 day old mature myocytes. The difference in the colocalization percentages between these two groups is small but statistically significant. Moreover, the colocalization could actually be higher in ventricular myocytes from earlier developmental stages but such measurements were not obtained. A difference in the location of colocalized voxels was also reported. Colocalized voxels were found predominately at the cell interior in adult cells whereas most colocalized voxels were concentrated at the cell surface in neonatal cells (76). Experimental results from these imaging studies demonstrate how spatial information can accurately predict functional changes by revealing the re-organization of protein proximity.

1.3.5 Restricted Microdomain

The notion that a restricted microdomain exists between the SL and junctional SR in ventricular myocytes, to facilitate E-C coupling, has received much attention. It is hypothesized that this restricted space, often referred to as the "fuzzy space", establishes an intracellular Ca^{2+} gradient, where different local $[Ca^{2+}]$ can exist in different cellular compartments (81-83). For example, Stern et al. suggested the Ca^{2+} levels in this microdomain may be one order of magnitude higher than the bulk phase $[Ca^{2+}]_i$ (84).

Support for this hypothesis came from the observation that there is a time delay between I_{NCX} and the Ca^{2+} transient. Trafford et al. reported in adult rat ventricular myocytes,

there was a time delay of 133 ms between I_{NCX} and the Ca^{2+} transient (82). More recently, Huang et al. also demonstrated a time delay between I_{NCX} and the Ca^{2+} transient in rabbit ventricular myocytes (40). In fact, Huang et al. found that this time delay is highest in 3 day old neonatal cells (287 ± 64 ms), and the time delay decreases drastically during development, reaching only 64 ± 13 ms in 56 day old cells.

More direct imaging evidence for the existence of these restricted microdomains came from electron micrographs showing the SR organization in rabbit ventricular myocytes. The SR network in these 56 day old myocytes adopts a tubular-like appearance where the length along the tubules is measured to be near 100 nm (44). In contrast, SR in the 3d myocytes appear to form sheet-like structures extending along the SL, averaging at ~300 nm in length, a value that is 3 times longer than that observed in the 56 day old myocytes. This narrow longitudinal restricted cleft may in turn explain the periphery concentrated distribution of NCX-RyR colocalized voxels.

Even if NCX and RyR do in fact co-exist in this proposed restricted microdomain, the gating of RyR mediated by NCX may require more than the spatial proximity of these two proteins. As discussed in section 1.2.3, local increases in $[Na^+]$ can result in Ca^{2+} influx through reverse mode NCX (33). Considering the reversal potential of NCX, the presence of Na^+ channels is likely important in promoting reverse mode NCX activity. Additional evidence supporting a functional association between Na^+ channels, NCX, and RyR came from guinea pig myocytes, where the activation of Na^+ channel caused a Ca^{2+} influx via NCX as well as NCX-CICR (85). Recently, Poburko et al. (2007) also demonstrated in stimulated rat aorta smooth muscle cells that Na^+ influx through the transient receptor potential canonical channel 6 (TRPC6), results in localized $[Na^+]_i$ elevation at the cell periphery and

can facilitate NCX-mediated Ca^{2+} influx (86). Despite the available functional evidence, direct spatial information obtained from imaging studies in adult rat ventricular myocyte reported that NCX, Na^{+} channels, and RyR are not localized in the same microdomain (20). These differences could reflect species or cell type differences as well as technique limitations, and will require further investigation.

1.4 Caveolae

Caveolae were first identified by electron microscopists more than 50 years ago (87,88). These peculiar structures were first described as narrow-necked plasma membrane invaginations ranging from 50 to 100 nm in diameter and appeared "smooth" in electron micrographs, distinct from the larger coated vesicles such as clathrin coated pits. The definition of caveolae has since been expanded to include vesicles detached from the plasma membrane, often arranged in grape-like clusters or even fused into elongated tubules (89,90). Caveolae are not only morphologically identifiable, they are also biochemically distinct from the surrounding plasma membrane, possessing specialized protein and lipid compositions.

Lipid composition heterogeneity and the clustering of certain lipids in biological membranes were first demonstrated more than 20 years ago (91,92). Subsequently, the discovery of glycosylphosphatidylinositol (GPI) anchored proteins, demonstrated that the clustering phenomenon also applies to some membrane proteins (91-93). Around this time, the idea of lipid rafts as highly-ordered microdomains residing within the plasma membrane was developed. In 1992, a group demonstrated that cell membranes are not completely solubilized by non-ionic detergent at cold temperatures and the lower density insoluble lipid fractions contain GPI-anchored proteins (94). This set of pivotal experiments not only lent support to the lipid raft hypothesis, but also showed for the first time that these microdomains are biochemically distinguishable. More recent studies have more precisely defined the lipid composition of lipid rafts to be enriched in cholesterol, glycosphingolipids, and sphingomyelin (95-97). Given the similarities in the lipid compositions and biochemical properties, caveolae have traditionally been considered as a subset of lipid rafts.

Ultrastructurally, the presence of caveolae have been identified in many tissues and cell types including lung tissues, adipocytes, endothelial cells, fibroblasts, smooth muscle cells, skeletal muscle cells, and cardiac muscle cells, all at differing levels (98-101). Such diverse tissue specificity and expression levels suggest a wide range of cellular functions. Indeed, caveolae have been implicated in many cellular processes including vesicular transport, cholesterol homeostasis, signal transduction, tumour suppression, and Ca^{2+} homeostasis. Similarly, emerging data from the lipid raft field have also indicated the possible involvement of specialized lipid rafts in these processes, thus further strengthening the link between caveolae and lipid rafts.

1.4.1 Caveolins

The molecular makeup of caveolae was not elucidated until long after the initial discovery. The original protein marker of caveolae, caveolin-1 (cav-1), was discovered in an antibody screen for tyrosine-phosphorylated substrates in Rous sarcoma virus-transformed fibroblasts (102). Subsequent experiments identified this 22 kDa protein as the major structural protein of caveolae (103). Since the initial characterization of caveolin, two additional members of the caveolin gene family have been discovered. Caveolin-2 (cav-2) was discovered by sequencing a 20 kDa protein that co-purified with adipocyte-derived caveolar membranes (104) whilst caveolin-3 (cav-3) was identified through database searches and traditional cDNA library screening for cav-1 homologous genes (105,106).

Of the three proteins, there is a relatively high degree of identity between cav-1 and cav-3 at 65% (85% similarity), whereas cav-2 is the most divergent, showing only 38% identity, and 58% similarity to cav-1 (107). Nevertheless, in most species examined, all three proteins contain a stretch of amino acid sequence “FEDVIAEP”, now commonly

referred to as the caveolin signature motif. To date, the structural or functional significance of the caveolin signature motif remains unknown.

Caveolins are unconventional membrane-spanning proteins that can exist as a monomer, homo-oligomer, or hetero-oligomer. Cav-1 is ubiquitously expressed, although at different levels (108) and exist as 14-16 oligomeric complexes migrating at 200-400 kDa (109). Cav-3 also forms large oligomeric complexes of approximately 350-400 kDa. However, cav-3 is found exclusively in muscle cell types, namely the skeletal, cardiac and smooth muscle cells (105). Interestingly, cav-2 is only found in cav-1 expressing tissues (104) and requires cav-1 to participate in the formation of high-molecular-mass complexes (110). Thus cav-1 not only forms large homo-oligomeric complexes in vivo, cav-1 and cav-2 can also interact to form stable high molecular weight hetero-oligomers.

After summarizing the available experimental data, Razani el al. (111) presented the primary structure and the predicted membrane topology of cav-1 (see Figure 3). In their model, cav-1 assumes an incomplete hairpin structure where both the amino and carboxy termini are oriented towards the cytosolic face of the plasma membrane. In total, excluding the 2 terminal domains, 4 protein domains are identified in cav-1: the carboxy-terminal membrane attachment domain, the transmembrane domain, the amino-terminal membrane attachment domain (also called the caveolin scaffolding domain), and the oligomerization domain. Both membrane attachment domains are important in the correct targeting of the protein. The caveolin scaffolding domain is important in mediating interaction between caveolins and associated signalling molecules. As the names suggest, the transmembrane domain spans the lipid bilayer whereas the oligomerization domain is important in assembly of oligomers. The oligomerization domain also houses the caveolin signature motif.

Although no such model has been proposed for cav-3, due to the high degree of sequence identity between cav-1 and cav-3 proteins, cav-3 is presumably organized in a similar fashion.

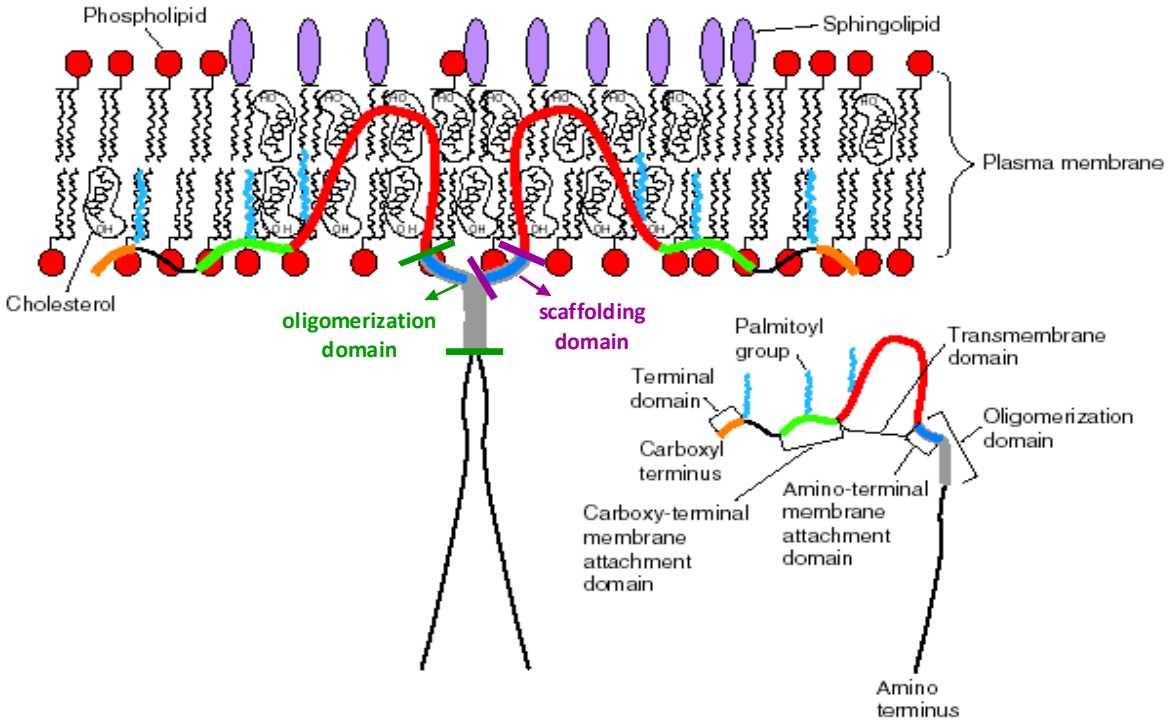

Figure 3: Caveolin-1 membrane topology and organization in a lipid bilayer.
Two caveolin-1 molecules are shown as homo-dimers inserted into the lipid bilayer. Interaction between caveolin-1 monomers are mediated via the oligomerization domain. Scaffolding domain has been shown to interact with a variety of protein partners including signalling molecules. Membrane attachment domains are responsible for anchoring caveolin-1 in the lipid bilayer. The transmembrane domain spans the lipid bilayer. Adapted from Razani et al. (111).

1.4.2 Caveolae in Signal Transduction

To investigate the cellular functions of caveolae, several groups attempted to analyze the identity of resident caveolar proteins. Taking advantage of the insolubility of caveolae in mild detergents and the high buoyancy of caveolae in sucrose density gradients, caveolar membrane was biochemically isolated. Subsequent analyses showed that caveolae associated proteins include G-protein-coupled receptors (GPCR), ion channels, adaptor proteins and structural proteins. In particular, a large majority of the proteins found in caveolae were signal transduction molecules (112,113).

In 1994, Lisanti et al. (114) proposed a caveolae/lipid raft hypothesis that argues the compartmentalization of signalling molecules in caveolae provides a mechanism for temporal and spatial signal transduction and allow for cross-talk among different signalling pathways. For example, both β1 and β2 adrenergic receptors as well as the downstream effector of the adrenergic pathway, adenylyl cyclase type 6, localize to the caveolae (115-118). Other GPCR such as muscarinic and μ-opioid receptors are also associated with caveolae (117,119).

Of all signalling molecules modulated by caveolae, endothelial nitric oxide synthase (eNOS) is probably the one studied most extensively. Under resting conditions, eNOS activity is inhibited through binding to the scaffolding domain of caveolin. Increases in the cytosolic calcium concentration disrupt this interaction between eNOS and caveolin, effectively increase eNOS activity (120-122). In general, caveolins may function as negative regulators inhibiting the basal activity of signalling molecules until activation of such signalling pathways. Although many signalling proteins have been localized to caveolae, different experimental techniques have also produced conflicting evidence for some proteins.

Thus the precise roles of caveolae in different signal transduction pathways remain controversial.

1.4.3 Caveolae in Vesicular Transport

Caveolae also appear to mediate the selective uptake and transport of several molecules via different vesicular transport processes including transcytosis, endocytosis, and potocytosis. Transcytosis refers to the process of transporting proteins from the luminal side of an endothelial cell to the interstitial compartment. Labeling experiments with antibody specific to the extracellular domain of caveolar resident proteins showed that these antibodies can cross the capillary wall directly through caveolae at a much more rapidly rate than diffusion alone, providing evidence for caveolae-mediated transport as a kinetically favourable route of transcytosis for certain proteins (123).

In caveolae-mediated endocytosis, after detachment from the plasma membrane, internalized caveolae fuse with various intracellular compartments such as the endosomes, the ER, or the Golgi network. The first evidence for caveolae-mediated endocytosis came from the observation that caveolins can traffic from the plasma membrane to the ER or Golgi compartment (124). Internalizations of additional proteins including alkaline phosphatase have also been shown to occur via caveolae (125). Even some toxins such as cholera and tetanus can be internalized through this pathway (126). Several organisms also seem to have developed strategies exploiting the caveolae endocytotic pathway to gain entry into the cell. Both simian virus 40 and some *Escherichia coli* strains have been shown to enter cells via receptors found in the caveolae (127-129).

On the other hand, potocytosis is the process by which cells can transport small molecules less than 1 kDa without having to endocytose vesicles to internal endosomal or

lysosomal compartments. Anderson et al. (130) demonstrated how caveolae can facilitate the uptake of folate by closing their necks, creating a highly concentrated pool of folate in the caveolar space while the caveolae still remain associated with the plasma membrane. The folate molecules are then transported into the cytoplasm by carriers present in the caveolar membrane (131). Evidence for this pathway involving other small molecules is still needed to establish the precise physiological contribution of this process. In addition, more mechanistic details are required to better define this process.

1.4.4 Caveolae in Oncogenesis

The initial discovery of cav-1 in transformed embryonic chicken fibroblasts was pivotal in two ways. It instigated experiments that led to: 1) the identification of the caveolins, and 2) the implicated role of caveolae in oncogenesis (132). Many subsequent studies recognized a transcriptional down-regulation of cav-1 and ablation of morphologically identifiable caveolae in tumour-derived cell lines and primary carcinomas (133-137). The down-regulation of cav-1 in these cells suggests that cav-1 may be a direct target of activated oncogenes. In fact, the battle between oncogenes and cav-1 is hardly one-sided. Cav-1 is also a potent inhibitor of oncogenes or effectors in the pro-proliferative signalling pathways. For example, cav-1 has been shown to inactivate c-Neu, c-Myc, platelet-derived growth factor receptor, and phosphatidylinositol 3-kinase (133,135,138-140). Furthermore, down-regulation of cav-1 via the application of either antisense or RNA interference (RNAi) leads to the mitogen-activated protein (MAP) kinase cascade hyperactivation phenotype of cellular transformation (141,142). Similar in vivo evidence exists in parallel. In many human epithelial tumours such as breast (143), prostate (144), ovarian (145) and colon cancers (146), the genetic loci housing cav-1 and cav-2 are

frequently deleted. In support of this notion, some mutations in the cav-1 gene have been found in human breast cancer samples (147).

1.4.5 Caveolae in Cholesterol Homeostasis

The first set of clues suggesting a role for caveolae in cholesterol homeostasis came from studies using cholesterol chelating agents. Application of these agents flattens the caveolae on the plasma membrane (103). The results suggest that cholesterol is probably an essential component in the formation of caveolae. Given the fact that 90% of cellular cholesterol is stored at the plasma membrane, this result is not surprising (148). Subsequently in 1996, Smart et al. (149) showed that *de novo* synthesized cholesterol are first transported to the caveolar membrane then distributed to the rest of the plasma membrane. Furthermore, cav-1 was found to be important in the binding and delivery of cholesterol to caveolae (150,151).

Not only are caveolae important in the intracellular cholesterol transport, caveolae are also involved in cholesterol efflux from cells. Excess free cholesterol in the cell is removed by transferring it from the outer leaflet of the plasma membrane to high-density lipoproteins in the extracellular space, which then carry cholesterol to the liver. This process is referred to as reverse cholesterol transport (152). The same group demonstrated caveolae as the sites of cholesterol efflux in reverse cholesterol transport (153). In fact, the actual cholesterol transfer process is likely mediated by the class B type I scavenger receptor, SR-BI, found concentrated in the caveolae (154-157).

1.4.6 Caveolae in Ca^{2+} Homeostasis

Caveolae have a specialized function, Ca^{2+} homeostasis, in striated muscle cells. To date, the majority of available experimental data suggests such by substantiating an association between cav-3 and protein components of the Ca^{2+} handling system. For example, $Ca_v1.2$ (158,159), plasma membrane Ca^{2+} pump (159), $K_v1.5$ voltage-gated K^+ channel (160), voltage gated Na^+ channels (161), and RyR (162) have all been found to co-immunoprecipitate (co-IP), co-fractionate, or colocalize with cav-3. However, these morphological and biochemical information offered no mechanistic details on how caveolae modulate Ca^{2+} homeostasis.

More recently, functional data showed more specifically that, caveolae modulate E-C coupling by modulating the efficiency of CICR, rather than altering Ca^{2+} influx (163). Calaghan et al. demonstrated how the application of methyl-β-cyclodextrin, a caveolae disrupting agent, reduced fractional SR Ca^{2+} release, Ca^{2+} transient amplitude, and cell shortening, but not L-type current (I_{Ca}) or the SR Ca^{2+} load in adult rat ventricular myocytes. Another group demonstrated that methyl-β-cyclodextrin treatment on neonatal rat cardiomyocytes eliminated Ca^{2+} sparks (164). This led to the hypothesis that $Ca_v1.2$ is localized in caveolae prior to T-tubule development, forming a CICR unit with an adjacent RyR. It is not inconceivable that one such structure involving NCX also exists in neonatal cardiomyocytes, particularly given the functional and spatial evidence implicating the existence of NCX-CICR in neonatal ventricular myocytes as discussed in section 1.3.3. While entertaining the idea that caveolae may house CRUs, one must also consider the nature of the experimental techniques used. The use of methyl-βcyclodextrin is a relatively

crude technique that may have the undesirable effect of altering other cellular properties in addition to the cellular localization of cholesterol.

Caveolae have also been implicated in T-tubule biogenesis. As discussed in section 1.3.1, T-tubules are absent at birth and gradually develops during ontogeny. Initial electron microscopy analysis of caveolae led to the hypothesis that the T-tubule system forms via the fusion of numerous caveolae (165). More recently, mutations in cav-3 have been found in patients with muscular dystrophy (166). Histological and electron microscopy examinations revealed that the muscle cells in these patients exhibit impairment in caveolae formation (97,167). After the identification of caveolins, cav-3 was also found to be transiently associated with T-tubules during development in skeletal muscle cells (89). Cav-3 knock out data show that T-tubules do form in these cav-3 null mice but some T-tubule abnormalities do exist in the muscle fibres (168). Thus Minetti et al. (167) concluded that cav-3 is essential for the formation and organization of caveolae in human muscle. Most of the available experimental data implicating caveolae to T-tubule genesis were obtained from skeletal muscles. For this reason, the role of caveolae or cav-3 in T-tubule formation of ventricular myocytes has not been well characterized. In 2002, Woodman et al. (169) investigated the hearts of cav-3 knockout mouse and found that these mice develop a progressive cardiomyopathic phenotype including hypertrophy, left ventricular wall thickening, chamber dilation, reduced systolic function, interstitial fibrosis and altered signalling pathway. Unfortunately, no detailed analysis regarding the T-tubule phenotype was performed on these individual ventricular myocytes. Thus, more studies employing different techniques are needed to precisely define caveolae involvement in cardiac E-C coupling.

1.5 Research Hypothesis and Objectives

1.5.1 Overall Hypothesis

Caveolae are the structural microdomains responsible for organizing NCX into high density protein clusters in close proximity to RyR in neonatal ventricular myocyte. Thus at least a subpopulation of NCX is colocalized with cav-3 in the early developmental stages, and such colocalization declines as ventricular myocytes mature into adulthood.

1.5.2 Research Objectives

1) To determine changes in cav-3 distribution and spatial organization during development.
2) To determine changes in NCX distribution and spatial organization during development.
3) To determine changes in the spatial relationship between cav-3 and NCX during development.

CHAPTER II: MATERIALS AND METHODS

2.1 Animals

New Zealand White rabbits of either sex from five different age groups (days post-partum): 3d, 6d, 10d, 20d, and 56d were used in this study. For each age group, at least 3 hearts and 10 cells per heart were studied.

2.2 Cell Isolation

Ventricular myocytes were isolated by a procedure previously described (40). All solutions were prepared with double deionized water prepared by a Milli-Q water system and filtered with a 0.2 μm filter (Nalge Company, NY, USA). The solutions were aerated with 100% O_2 before and during the isolation.

Rabbits were injected with pentobarbital sodium (65 mg/kg body weight) and heparin (15 mg/kg body weight) either intraperitoneally for neonates or intravenously for adults. Hearts were then excised and kept in 4^{o}C Ca^{2+} free Tyrode solution for 1 minute to arrest the heart. After the pericardium was removed, the hearts were mounted on a Langendorff apparatus and retrogradely perfused first with collagenase (Yakult, Tokyo, Japan) in Ca^{2+} free Tyrode solution and then with protease (Sigma-Aldrich Canada, Oakville, ON) in storage solution. Bovine serum albumin was also added to both collagenase and protease solutions to give a final concentration of 1%. The perfusion speed, digestion time, and enzyme concentrations were optimized for each age group. After digestion was completed, the hearts were transferred into a Petri dish containing storage solution where ventricles were dissected from the rest of the heart. The ventricles were then cut into small pieces to release

individual myocytes. The cell suspension was filtered through a 200 μm coarse nylon mesh to remove tissue chunks while allowing individual cells to pass through. The majority of isolated myocytes retain good morphology and myocytes are distinctly identifiable by visual inspection.

2.3 Antibodies

The primary antibodies used were monoclonal anti-caveolin-3 IgG_1 antibody (610420, BD Biosciences, Mississauga, ON, Canada), and monoclonal anti-NCX IgM antibody (MA3-926, Affinity Bioreagents, Golden, CO). Secondary antibodies were affinity purified, isotype-specific goat polyclonal antibodies that were either anti-mouse IgG_1 conjugated to Alexa Fluor 488 (A21121, Invitrogen Canada, Burlington, ON) or anti-mouse IgM conjugated to Alexa Fluor 555 (A21426, Invitrogen Canada, Burlington, ON). These secondary antibodies react specifically with the F_c portion of the immunoglobulin heavy chain of the appropriate isotype, thereby allowing for distinction between the two mouse-derived monoclonal antibodies. To minimize cross-reactivity, these antibodies were also highly adsorbed against other antibody isotypes. Control primary antibodies raised against *Aspergillus niger* glucose oxidase, an antigen absent in mammalian cells, were obtained from DakoCytomation, Denmark (mouse IgG_1, X0931; mouse IgM, X0942).

2.4 Indirect Immunofluorescence Labeling

Isolated myocytes were prepared as described previously (76). All steps of cell preparation were done in 15 mL disposable polystyrene centrifuge tubes. During each

incubation, the tubes were gently agitated using an orbital shaker at 100 revolutions per minute (RPM) and cells were collected by centrifugation for 2 min at 10,000 RPM at the end of each incubation. Isolated ventricular myocytes were first fixed in 2% paraformaldehyde in phosphate-buffered saline (PBS), quenched in 0.75% glycine solution, permeabilized in 0.1% Triton X-100 solution in PBS, and washed in PBS for 3 times. Each one of the incubations was 10 min. Finally, prepared cells were settled onto poly-L-lysine (Sigma-Aldrich Canada, Oakville, ON) coated coverslips for 1 hr at an appropriate density.

Antibody solutions were applied directly onto the coverslips. Cells were first incubated in anti-caveolin-3 antibody diluted in antibody buffer (75 mM NaCl, 18 mM sodium citrate with 2% goat serum, 1% bovine serum albumin, 0.05% Triton X-100, 0.02% NaN_3) at 125 ng/mL for 4 hours at room temperature. Cells were then washed for 3 × 10 min in antibody wash solution (18 mM sodium citrate containing 0.05% Triton X-100) before incubating in anti-mouse IgG_1 conjugated to Alexa Fluor 488 (4 μg/mL) for 1 hour at room temperature. After 3 × 10 min washes, cells were incubated with anti-NCX IgM antibody (250 ng/mL) at 4^oC overnight. After the overnight incubation, cells were washed with 3 × 10 min washes before the last 1 hour incubation of anti-mouse IgM conjugated to Alexa Fluor 555 (4 μg/mL) at room temperature. To remove traces of detergent, after the final three 10 min washes in antibody buffer, cells were subjected to an additional 5 min wash in PBS before the coverslips were mounted onto frosted glass slides (Surgiglass, 1.00 mm thickness) in Slow Fade Gold anti-fade reagent (Invitrogen Canada, Burlington, ON) and sealed with nail polish.

Control primary antibodies were used to determine the level of non-specific staining of the isotype-specific secondary antibodies in these cardiomyocytes. Control cells were

stained as above using control primary antibodies of the same isotype at the same concentrations as their respective experimental primary antibodies (cav-3, IgG_1: 125 ng/mL; NCX, IgM: 250 ng/mL). Control images were acquired under the same acquisition settings as the experimental images. Only dim, diffuse staining was observed in these images. Single stain control experiments with mismatched secondary antibodies were used to determine the specificity of the secondary antibodies used (i.e. cav-3 + IgM; NCX + IgG_1). The staining pattern was also dim and diffuse, similar in appearance to the isotype matched control primary antibodies experiments.

2.5 Image Acquisition

Images of labelled cells were acquired on a Zeiss LSM 5 Pascal laser scanning confocal microscope equipped with a Zeiss 63X/1.4 Plan-Apochromat oil immersion objective. The acquisition software was LSM5 Pascal version 2.8 SP1. The 543 nm and 488 nm excitation beams were supplied by Helium-Neon and Argon lasers (Zeiss LSM5 Pascal laser module), respectively. To minimize signal bleed through, images were collected sequentially in multi-track mode. The light path for the 488 nm excitation light was as follows: a NFT 488 dichroic beam splitter was used to separate excitation and emission light. Emitted fluorescence light was directed to photomultiplier tube #2 (PMT2) by a secondary dichroic mirror, NFT 545. Before reaching the PMT, the emission light had to pass through a narrow band-pass filter (518 nm ± 13 nm). For the 543 nm excitation light, emission light was separated by a NFT 545 dichroic mirror and filtered by a 560 nm long-pass filter before reaching PMT1 (see Figure 4). The pinhole size was set to one Airy disc for each collection channel. A typical stack consisted of 40 to 80 serial 2D images with a voxel size of 100

nm×100 nm×200 nm (axial). These 2D images were exported as 16 bit TIFF images for subsequent processing and analysis.

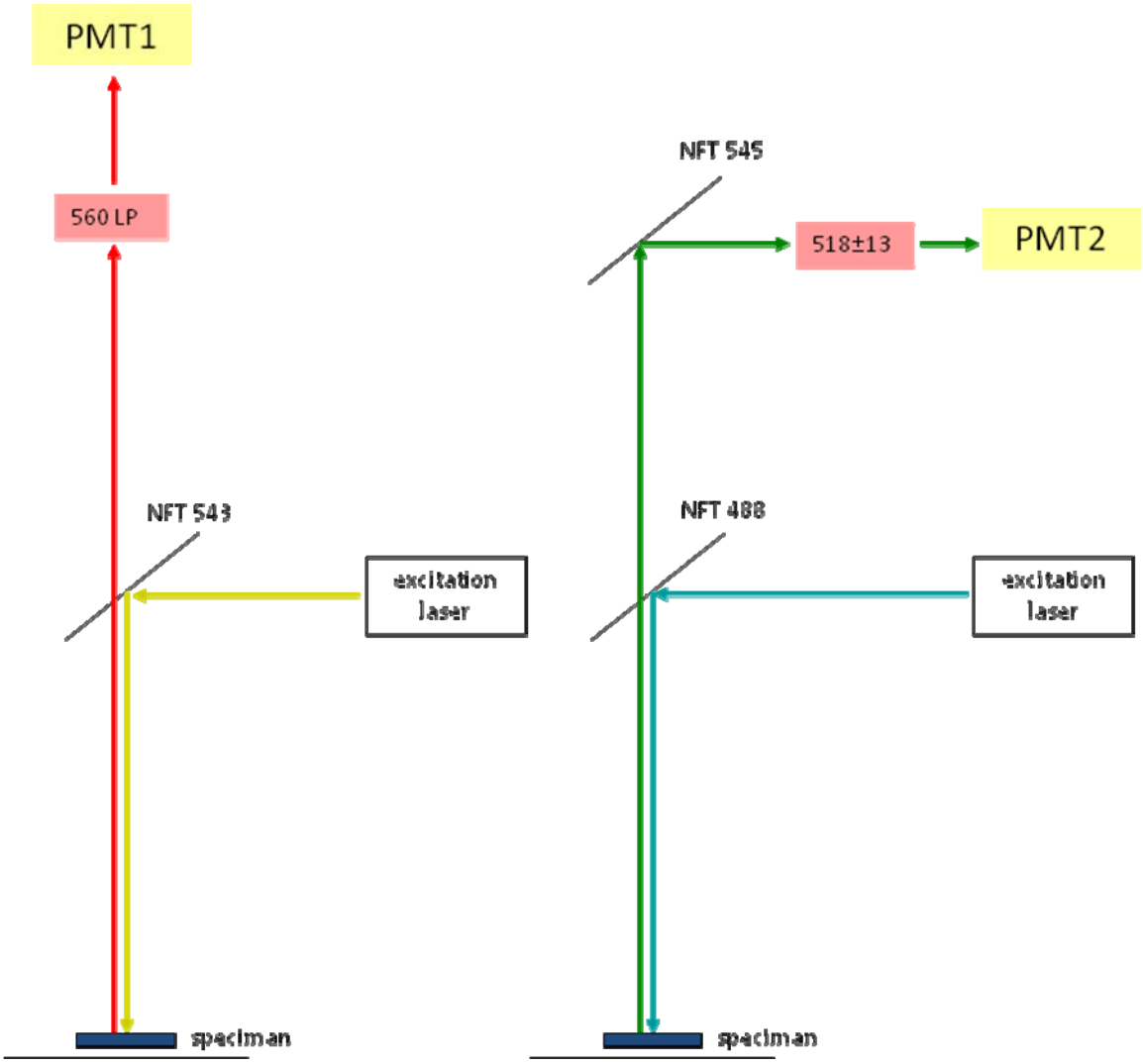

Figure 4: Confocal light path setup.
Optical light paths of the confocal microscope. For the 543 nm excitation line, emission light was separated from excitation light by a NFT 545 dichroic mirror and filtered by a 560 nm long-pass filter before reaching PMT1. For the 488 nm excitation light, a NFT 488 dichroic beam splitter was used to separation excitation and emission light. Emitted fluorescence light was directed to PMT2 by a secondary dichroic mirror, NFT 545. Before reaching the PMT, the emission light had to pass through a narrow band-pass filter (518 nm ± 13 nm).

2.6 Image Processing

2.6.1 Deconvolution

To optimize the resolution of the data, exported TIFF images were deconvolved using maximum likelihood estimation (MLE) algorithm in Huygens Pro 2.4.1 software (Scientific Volume Imaging, Hilversum, The Netherlands). The point spread function used during deconvolution was measured as described previously by Dan et al (76). Images of 220 nm diameter dual-coloured beads (Molecular Probes, custom order) were collected using a voxel size of 50 nm x 50 nm x 100 nm.

2.6.2 Cell Outline Extraction

The cell outline for each cell was estimated using a system of binary thresholds and morphological closing operations. Each label was manually thresholded to remove the majority of background signal and the two labels were then combined to generate a rough outline of the cell. It should be noted that this manual threshold value is independent of the automatic threshold determined based on object number as per section 2.6.5 and is only used for the purposes of determining the cell outline. Once the cell outline was determined, original images before the manual thresholding process were used for all subsequent image processing and analysis steps. To fill the interior of this outline as well as the gaps in the binarized image, morphological closing was used. Effectively, this morphological closing connects all pixels that are within a set radius of each pixel, forming an outline of the cell.

2.6.3 Noise Reduction

The process of cell outline extraction is highly sensitive to extraneous non-cellular fluorescence since morphological closing tends to include rather than exclude non-cellular

features. A single errant pixel can introduce large errors in the cell outline estimate. However, because the effects of errant pixels on the cell outline are systematic, we were able to create an "anti-noise mask" that could be used to eliminate the effects of these errant pixels. Because noise tends to be much smaller than the actual cell, morphological erosions can be used to eliminate objects that are smaller than a given diameter. By eroding cross-sectional images sequentially using a kernel (radius =1; 1 pixel layer), and then dilating sequentially with the same kernel, the anti-noise mask can be formed. To ensure the noise mask covers the entire cellular area, more dilations repeats were applied than erosion repeats. In our analysis, we used 7 erosion repeats and 10 dilations repeats to give us a separation distance of 3 voxels (some distance is required to avoid influencing the actual cell outline estimate). This anti-noise mask was then applied to the original NCX and cav-3 images and a new cell outline was generated (see Figure 5).

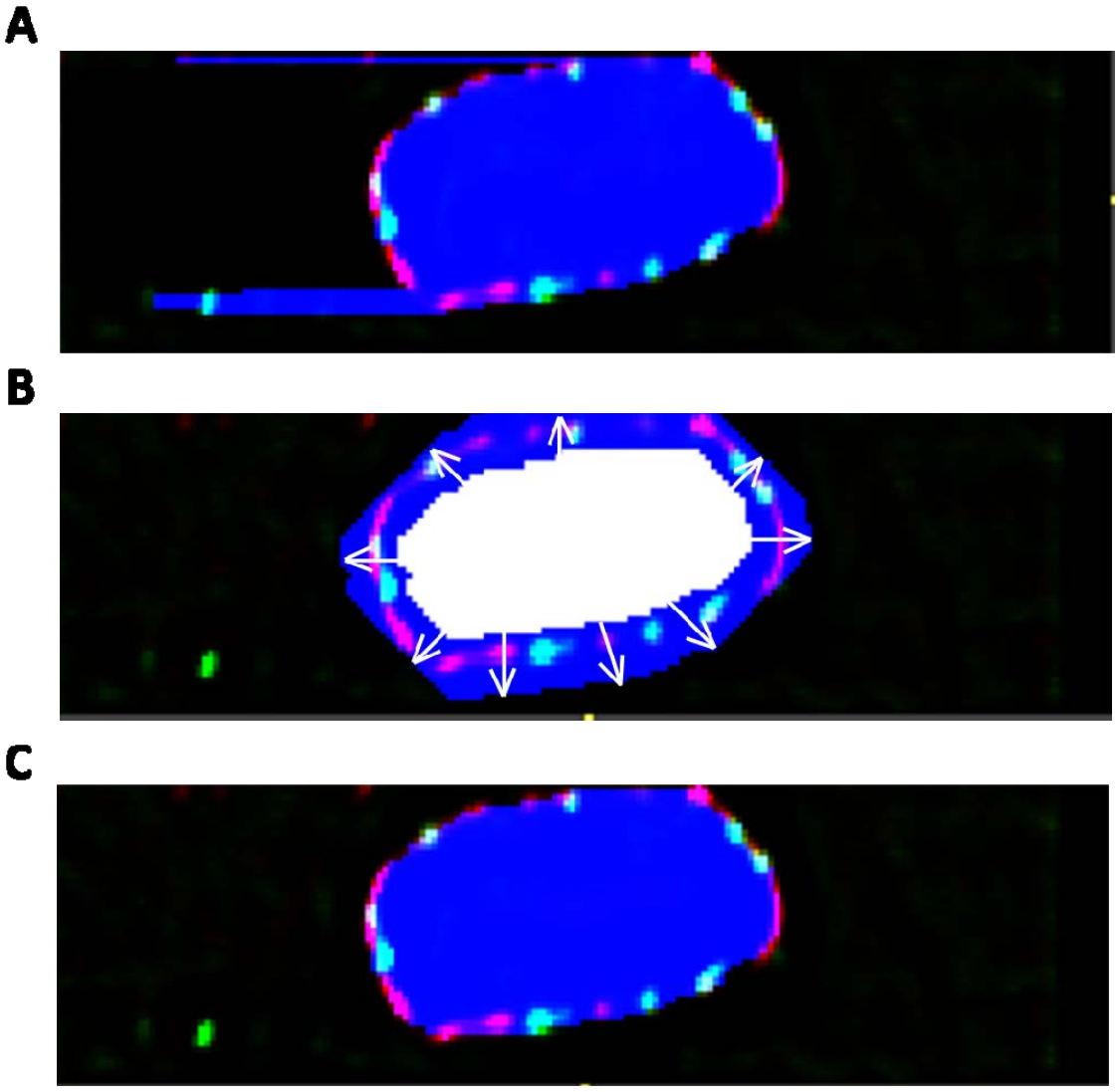

Figure 5: Cell outline extraction/noise reduction.

(A) Lit pixels away from the actual cell outline can introduce large errors to the automatic cell outline extraction process. In this cross-sectional image of a 6 day old myocyte, small errant pixels away from the actual cell obscure the initial cell outline estimate shown in blue.

(B) To exclude such noise, a noise mask shown in white is generated after 7 erosion repeats. The noise mask is then subject to 10 dilation repeats to arrive at a new noise mask shown in blue. Unlike the cell outline presented in (A), this noise mask excludes the effects of non-cellular image noise.

(C) Final cell outline is determined by applying the noise mask to the original image. Cell outline is now unaffected by the image noise.

2.6.4 Cell Layering and Assignment of Cellular Compartments

Once the cell outline for an image volume was obtained, the images were broken-down into individual layers by sequentially trimming a 1-pixel-thick sheet away from the cell outline. This was accomplished by repeatedly applying an erosion function on each cross-sectional image with a circular kernel (r=1). Each cell was segmented into a peripheral volume and an interior volume. The peripheral volume was defined as the first 3 layers of the cell outline, and the interior volume was defined as all layers inside the peripheral volume. The peripheral and interior volumes were used to estimate the characteristics of the peripheral sarcolemma and T-tubular space, respectively.

2.6.5 Thresholding by Number of Objects on Peripheral Sarcolemma

After assignment of the different cellular compartments, each peripheral volume was subjected to multiple threshold values ranging from 0 to 10,000 "intensity values" in 100 point increments (images were acquired as 16-bit images with a maximum intensity value of 65535). At each threshold value, the number of discrete objects was determined. Therefore, the number of NCX and cav-3 objects found on the periphery of the cell can be expressed as a function of threshold intensity. For each label, the threshold value that resulted in the maximal number of objects was used as the binary threshold for all subsequent analyses.

2.7 Image Analysis

2.7.1 Traditional Colocalization Analysis

Traditional colocalization calculations were used to describe the colocalization in three different cellular volumes: 1) whole cell volume, 2) peripheral volume, and 3) interior

volume, as designated in section 2.5.4. Only voxels containing both labels are considered colocalized. Colocalization percentage for each label was calculated by dividing the number of colocalized voxels by the total number of voxels containing that particular label per compartment.

2.7.2 Object-Specific Colocalization Analysis

In object-specific colocalization analysis, multi-voxel fluorescence clusters that did not contain any colocalization events were not considered in the calculation. Therefore, the object-specific colocalization percentage for any given compartment is the number of colocalized voxels divided by the total number of voxels in fluorescence clusters containing at least one colocalized voxel.

2.7.3 3D Distance Analysis

To obtain the 3D separation distance measurements, a binary reference image was created to record the 3D co-ordinates of each voxels in the surface volume. First, each fluorescence cluster on the surface volume was reduced to its centre of mass point. After which the cross-sectional images (YZ slice) of the surface volume was analyzed sequentially where the binary pixel intensity value (0 for not lit, 1 for lit) and the YZ co-ordinates of each pixel were recorded in the reference image. The top-left-most pixel in the volume in each cross-section is always the first pixel recorded. Thus, the top-left-most pixel of the first YZ slice corresponds to the reference square occurring at the first row and first column of the reference image. At the end of this process, the 3D spatial information of each voxel in the surface peel volume is successfully transferred to the compiled binary reference image.

For each centre of mass point, a set of neighbouring centre of mass points were found using the Delaney triangulation algorithm. To determine the separation distance between the central node and the neighbouring centre of mass points, connecting lines were drawn between the central node and each of the neighbouring points on the reference images. The XYZ co-ordinates of the connecting reference square along the connecting path were extracted. The separation distance along the curvature of the cell is the sum of the individual separation distances between each connecting reference square as determined by the XYZ co-ordinates.

Finally, filters were applied to discard points occurring outside of a 30 degree window along the longitudinal and transverse axes, with the long (longitudinal) axis of the cell positioned vertically. In each direction, three distances were calculated: 1) distance between two NCX clusters (NCX separation), 2) distance between two cav-3 clusters (cav-3 separation), and 3) distance between two neighbouring NCX and cav-3 clusters (NCX-cav-3 separation) (see Figure 6).

For internal events, distances were determined as per the surface distribution except instead of measuring the distance on the surface volume (2^{nd} peel layer), distances were measured on the 7^{th} peel layer. Because of the restricted space within the t-tubules, separation distances between NCX clusters and cav-3 clusters were not measured.

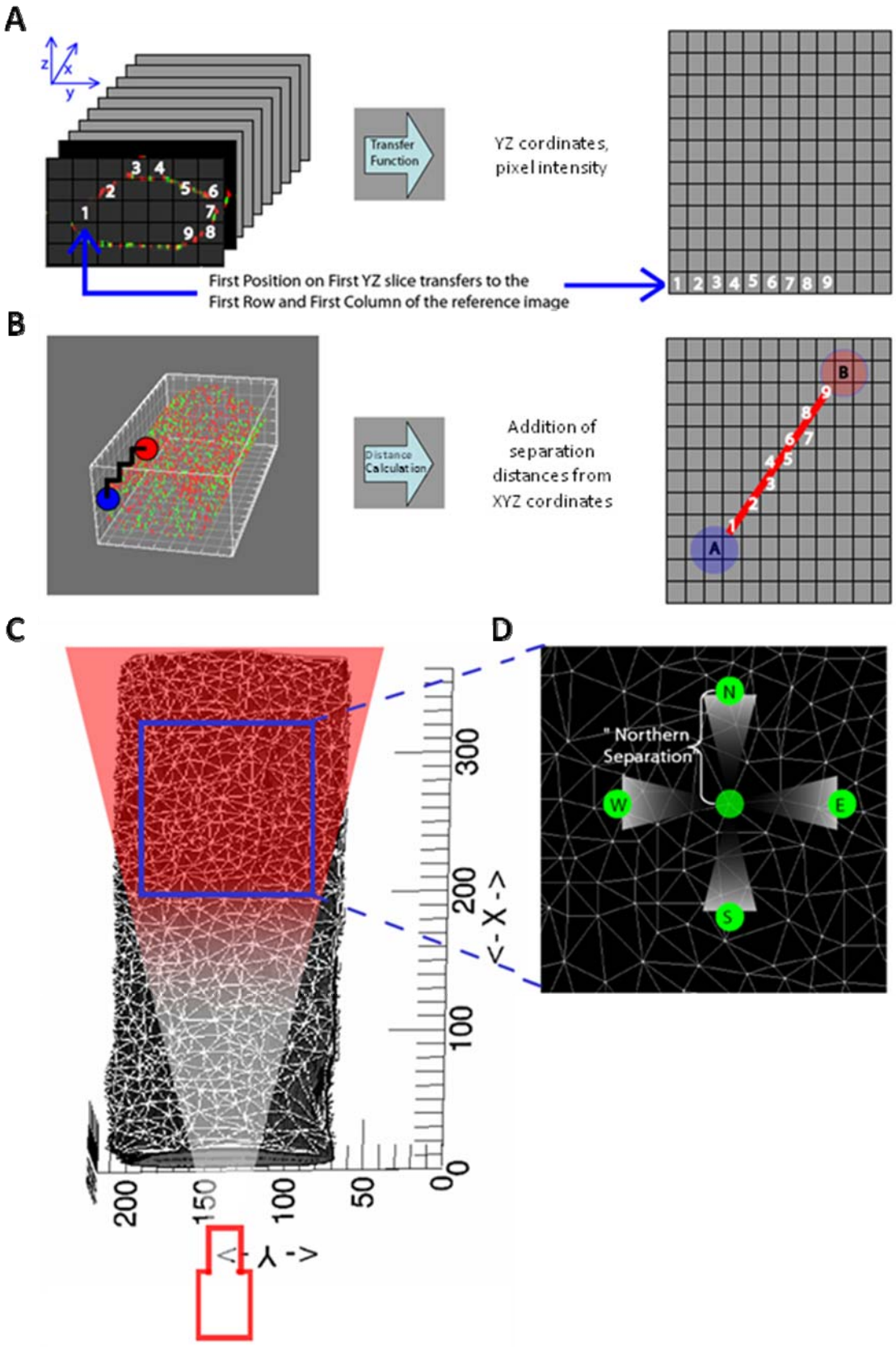
A
z
x
y
1
2
3
4
5
6
7
8
9
Transfer Function
YZ cordinates, pixel intensity
First Position on First YZ slice transfers to the First Row and First Column of the reference image
1 2 3 4 5 6 7 8 9
B
Distance Calculation
Addition of separation distances from XYZ cordinates
A
B
C
D
300
200
100
0
<- X ->
200
150
100
50
0
<- λ ->
N
W
E
S
" Northern Separation

Figure 6: 3D distance measurement methodology.

(A) 3D fluorescence information including the XYZ coordinates and pixel values from binarized, centre of mass determined, surface volume cross-sectional images are transferred into a 2D reference image.

(B) 3D separation distance of surface fluorescence clusters along the cell curvature are calculated by extracting the 3D coordinates of each of the reference squares on the reference image and determining the separation distance between each reference square. The total 3D separation distance between point A and point B are the sum of the separation distances from reference square 1 to reference square 9.

(C) Cell orientation for 3D distance analysis. This volume projection of peripheral NCX and cav-3 clusters shows with the long axis of the cell positioned vertically, Northern and Southern separations are defined as longitudinal separation distances while Eastern and Western separation are defined as transverse separation.

(D) Spatial filters are applied at final stages of the analysis to restrict analysis to points occurring within a 30 degree window (+/- 15 degrees) along the longitudinal and transverse axes.

2.8 Statistics

All statistical tests were done using single tail Student's t-test. Results were considered statistically significant when p-values are less than 0.05.

CHAPTER III: RESULTS

3.1 Thresholding Approach

Figure 7 is a representative threshold profile with corresponding NCX images at individual threshold values. At low intensity values, there were very few independent objects because the majority of clusters were connected by low intensity values. However, as the threshold intensity increased, more clusters became independent as the connective domains were removed. In the falling phase of each profile, the rising threshold intensity began to exclude clusters with lesser intensity. In each profile there was a range of intensities in which the number of objects for each label was relatively stable. Within this stable region, the thresholding intensity retained most small or dim objects without erroneously connecting brighter objects. Therefore, we selected a threshold value from this stable region for subsequent analyses.

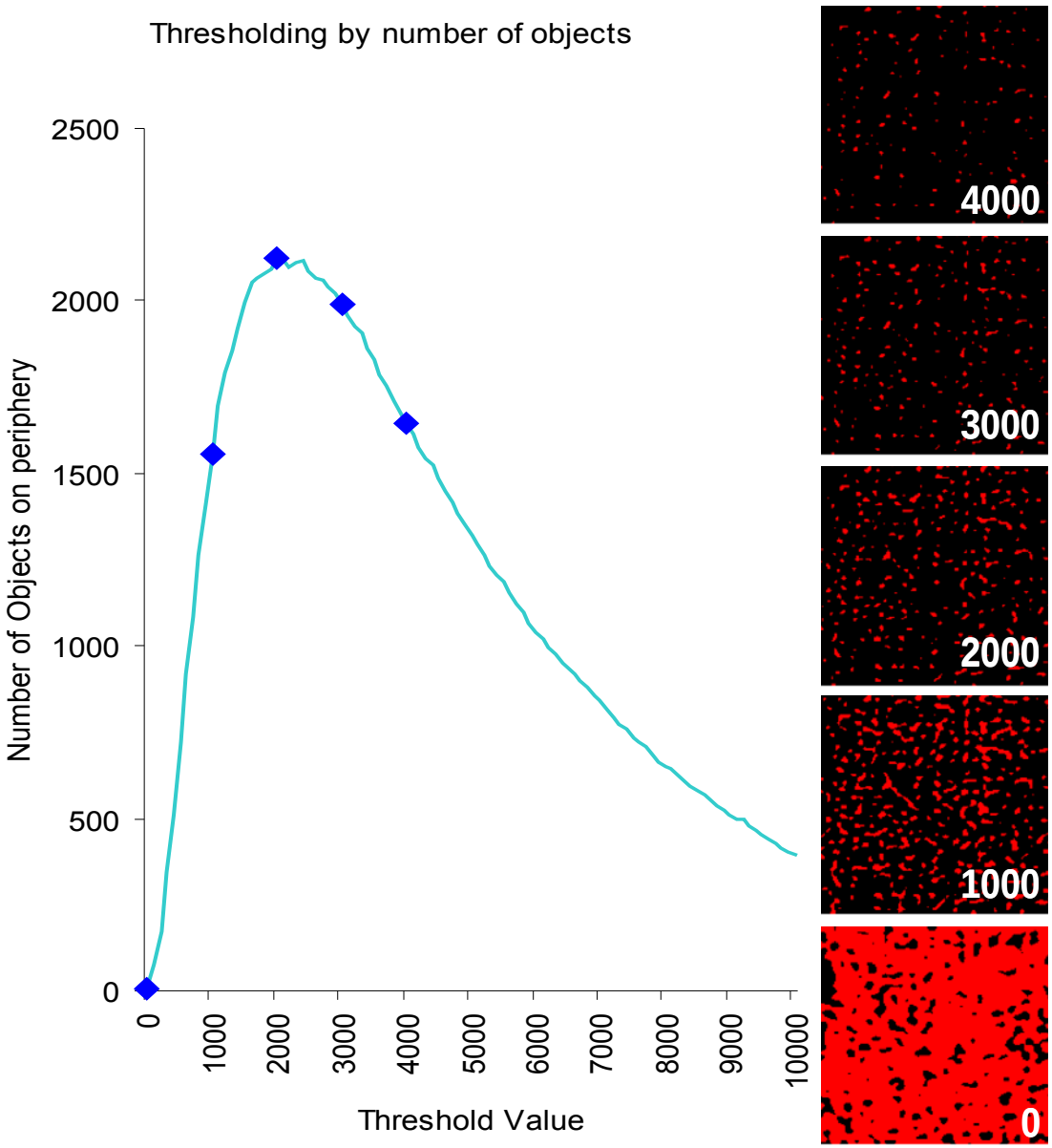

Figure 7: Image thresholding approach.
In the peripheral volume, the number of objects was determined at multiple threshold values for each label. Values ranging from 0 to 10000, in 100 point increments, were used. The peak value, where the maximal number of events occurred, was used as the binary threshold for all subsequent analysis. In this example, "2000" is the peak value with the maximal number of events. Images of the periphery at 5 different thresholding intensities are also shown. Note the connectivity between objects in "0" and "1000" and the loss of some objects at "3000" and "4000".

3.2 Protein Distributions During Development

Shown in Figure 8 are surface XY sections, middle XY sections and cross-sectionals of representative images for 3d, 6d, 10d, 20d, and 56d myocytes. Data obtained from 3d and 6d cells were indistinguishable; therefore 6d data are only presented graphically and omitted in the text. Surface images in Figure 8A show that the surface distributions of either label did not change with age. 3 day old myocytes had only minimal interior labelling, but by 10 days of age, both cav-3 and NCX labels were visible in the interior of the cell. As can be seen in the 20d and 56d middle XY sections, interior labelling progressively increased as the cells matured (Figure 8B).

The static surface distribution and progressive increase in interior labelling can also be seen in the cross-sectional images of Figure 8C. Visibly apparent in all three sets of images is the mutually exclusive relationship between NCX and cav-3 on the periphery of the cells for all developmental stages. This relation was later confirmed with 3D distance analysis.

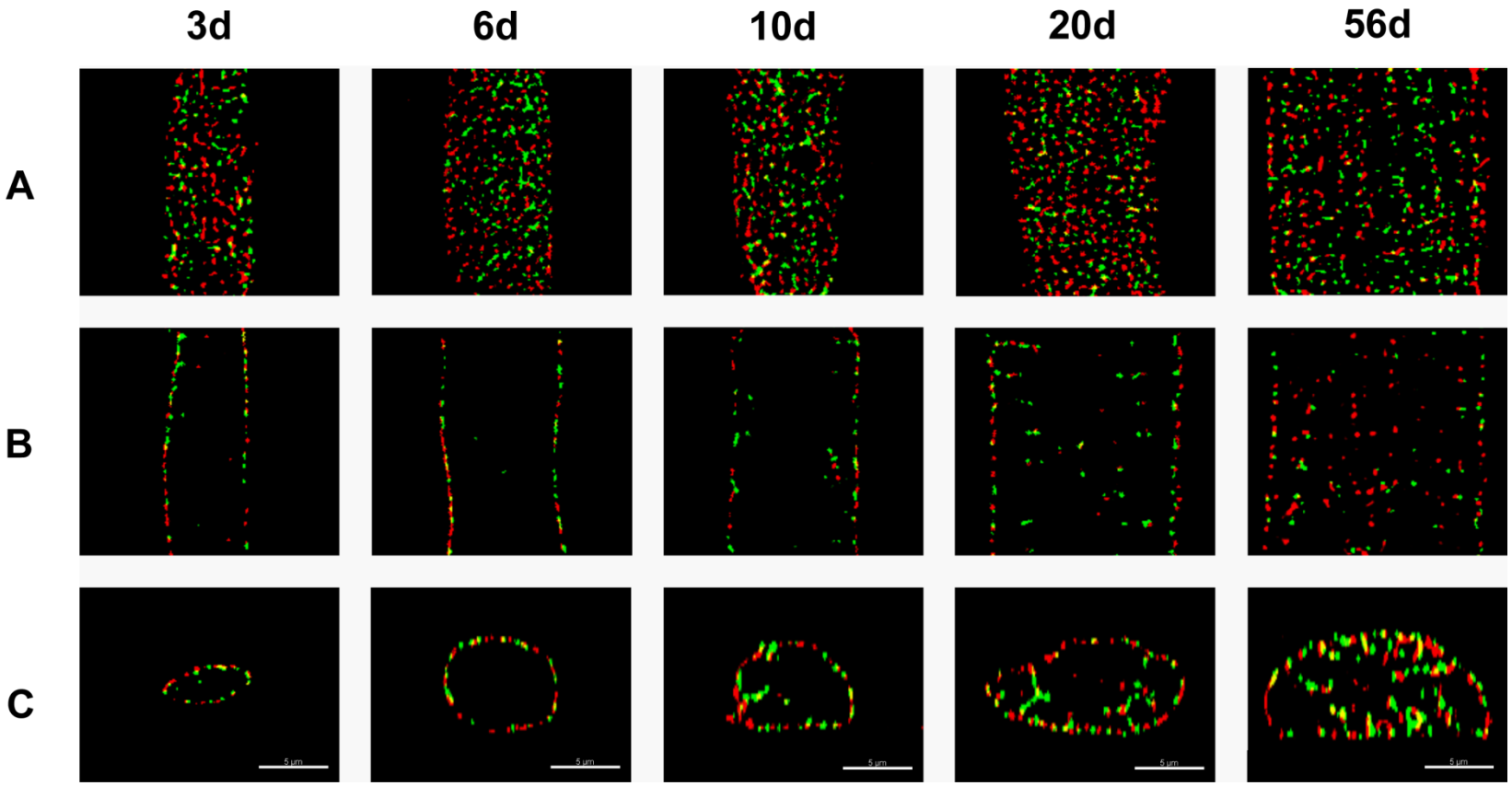
3d
6d
10d
20d
56d
A
B
C
5 µm
5 µm
5 µm
5 µm
5 µm

Figure 8: Distribution of cav-3 and NCX in developing ventricular myocytes.
Images of cav-3 (green) and NCX (red) labeled ventricular myocytes presented as:
(A) 800 nm thick xy surface sections,
(B) middle xy section (3 μm deep into the cell),
(C) 800 nm thick cross sections from 3d, 6d, 10d, 20d, and 56d old rabbits.
Both surface and cross section images are maximum intensity projections and colocalized voxels are displayed in yellow. Scale bar is 5 μm. Figures 8B and 8C demonstrate the alternating nature of the two protein labels both longitudinally and transversely.

3.3 Quantitative Colocalization Analyses

To quantitatively document these developmental changes, two types of colocalization analyses were used. Traditional binary colocalization revealed the colocalization percentages between NCX and cav-3 in the whole cell volume, peripheral volume alone, and interior volume alone. In addition, a novel colocalization technique, object-specific colocalization, was developed in this study. Object-specific colocalization considers each cluster of fluorescence as one object and specifically discards all objects that do not contain any colocalizing voxels. Colocalization percentages were then determined after removal voxels within non-colocalizing clusters. The primary rationale behind the development of this technique was to allow for the detection of small subpopulations of highly colocalized protein clusters typically overlooked by traditional colocalization analysis.

3.3.1 Traditional Binary Colocalization

The results of the traditional colocalization analysis and image segmentation are shown in Figure 9. For both labels, whole cell colocalizations in 20 day and younger age groups were all less than 15%. The 56d group had approximately 5% higher colocalization. Image segmentation separated the whole cell colocalization numbers into two categories: periphery and interior contributions. Peripheral contribution is defined as the number of lit

voxels in the peripheral volume divided by the number of total lit voxels in the whole cell volume, multiplied by the % of whole cell colocalization. Similarly, interior contribution is defined as the number of lit voxels in the interior volume divided by the number of total lit voxels in the whole cell volume, multiplied by the % of whole cell colocalization. It was determined that the colocalization increases in the 56d groups were due to increases in the interior colocalizations (Figure 9A and 9B). Independent analyses of the peripheral and interior compartments are shown in Figures 9C and 9D. The peripheral results did not show large changes with age, with only a 3-4% difference between the 3d group and the 56d group. However, the interior results showed a progressive increase during development. Note that the 3d interior contribution is shown for the sake of completion but was minimal in magnitude and was likely representative of errors associated with image segmentation.

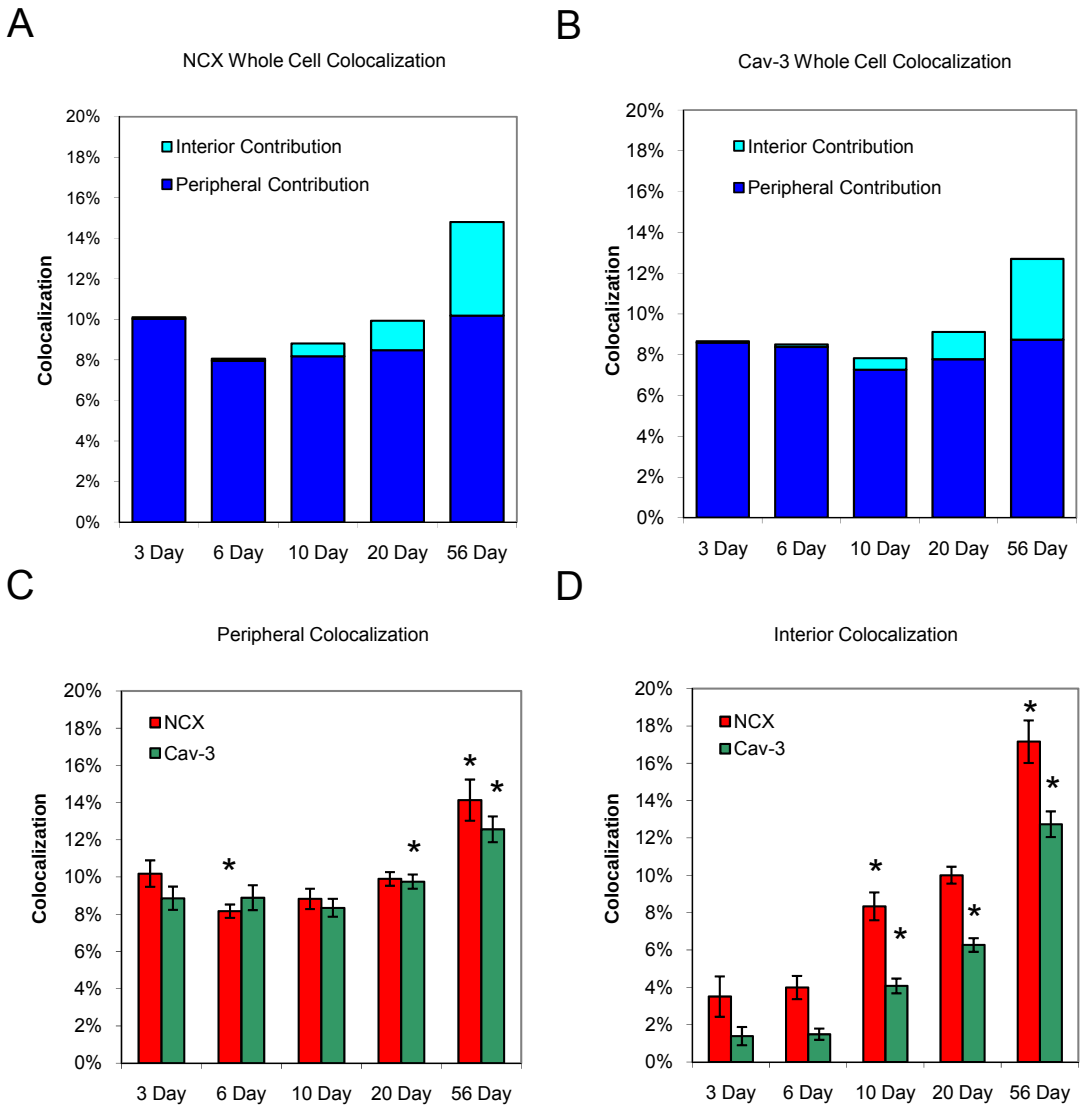

Figure 9: Traditional colocalization.
The peripheral and interior contributions of traditional whole cell colocalization for (A) NCX, and (B) cav-3. For both labels, the peripheral contribution of whole cell colocalization remains constant at around 10%. Increases in whole cell colocalization in older age groups were attributed to increases in interior contributions. The percentages of traditional colocalization were further broken down into the (C) peripheral volume, and (D) interior volume. Re-confirming results from (A) and (B), no significant developmental colocalization changes were found in the peripheral volume. Colocalization % increase steadily with development for both labels. (*) denotes a significant difference to the neighboring younger age group ($p < 0.05$).

3.3.2 Object-specific Colocalization

To test for the presence of a highly colocalized subpopulation, a novel object-specific colocalization analysis was used. The percentages of fluorescent clusters containing at least one colocalization event are shown in Figures 10A and 10B. In the peripheral volume, approximately 30% of all objects contain at least one colocalized voxel (Figure 10A). In this one-third of peripheral objects, all age groups had less than 20% colocalization, as shown in Figure 10C. In the interior, the percentages of interior objects containing at least one colocalization event range from 15 – 20% with a slight increasing trend with age (Figure 10B). The colocalization within these objects also exhibited slight increases with age from 10% to 20% for cav-3 and 20% to 30% for NCX (Figure 10D). Note that the NCX colocalization percentages of these colocalized voxel containing objects were consistently higher than that of the cav-3 label.

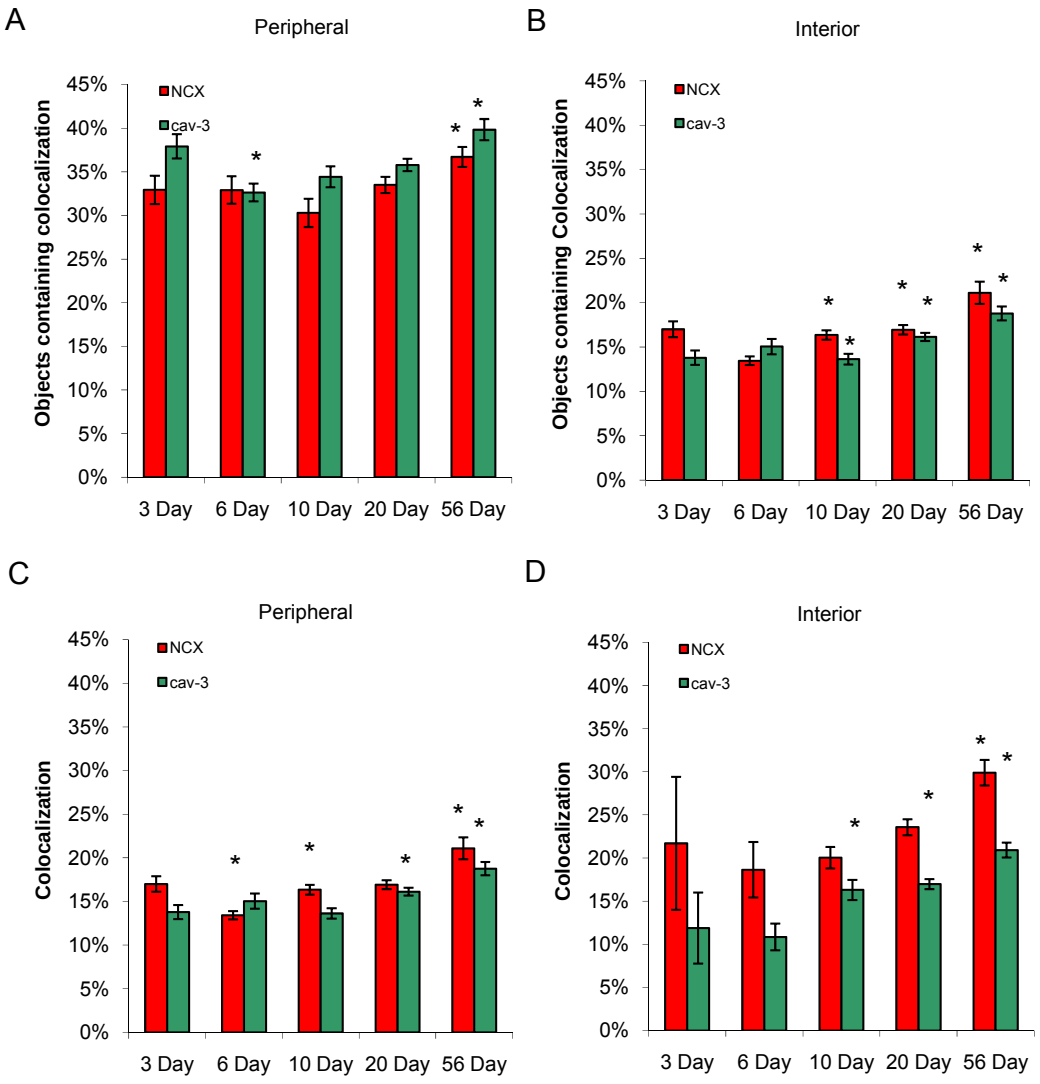

Figure 10: Object-specific colocalization.
The percentage of object clusters containing at least one colocalized voxel in the peripheral volume (A), and in the interior volume (B). Approximately 1/3 of peripheral objects and 15 – 20% of interior objects contain at least one colocalized voxel. Within the objects containing colocalized voxels, the percent colocalization for the peripheral and interior volumes are shown in (C) and (D) respectively. (*) denotes a significant difference to the neighbouring younger age group ($p < 0.05$).

3.4 3D Distance Analysis

Although no appreciable colocalization was detected between NCX and cav-3, quantitative observation suggests that a robust spatial relationship between these two proteins likely still exists. To better describe this spatial relationship, a 3D distance analysis technique was developed. Each fluorescence cluster was reduced to a single point based on the centre of mass and assigned a set of 3D coordinates. Peripheral separation distances between each fluorescence cluster were determined in 3D space along the curvature of the cell. Interior separation distances were also calculated in 3D space.

3.4.1 Peripheral Distribution

Shown in Figure 11 are the normalized results from the 3D distance analysis. Separation distances under 3 μm were normalized so that the area under each curve equals one. As mentioned in section 2.6.3, East and West separation distances were considered transverse and North and South distances were considered longitudinal. The mean plots for each age group are not shown due to the high degree of overlap for all distances measured. Due to this overlap, the transverse and longitudinal events were cumulated across all 5 age groups for display purposes. On the periphery, the NCX separation distance profile was found to be very similar to the cav-3 separation distance profile. However, the NCX-cav-3 distance profile appeared left shifted, indicating that NCX often has a cav-3 neighbour closer than another NCX cluster (Figures 11A, 11B).

3.4.2 Interior Distribution

Interior longitudinal and transverse separation distances are shown in Figures 11C and 11D, respectively. Since interior labelling was minimal in the young age groups, only

events from 20d and 56d were included in the interior distance analysis. Transverse frequency profiles for NCX and cav-3 separations appeared similar to the peripheral distribution. However, the interior longitudinal profile shows a bimodal distribution with a small peak near 1 μm and a larger peak at around 2 μm.

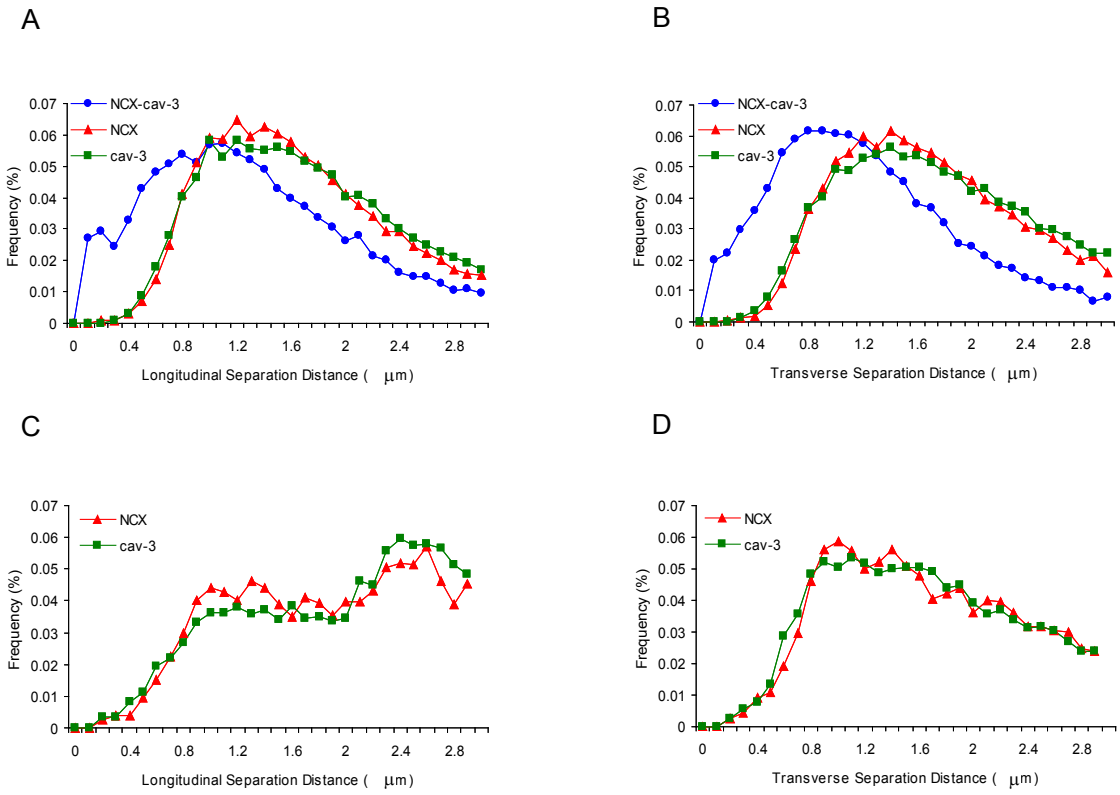

Figure 11: 3D distance analysis.
Peripheral separation distances between two NCX clusters, two cav-3 clusters, and one NCX cluster to the nearest cav-3 cluster in (A) longitudinal and (B) transverse directions. All cells were included for the peripheral measurements. Interior longitudinal separation distances are shown in (C) and interior transverse separation distances are shown in (D). Since interior labelling is minimal in young age groups, (C) and (D) represent data from 20d and 56d only (N = 50 and 23 respectively).

CHAPTER IV: DISCUSSION

4.1 Protein Distributions

4.1.1 NCX distribution

In this study, we found that NCX distribution is initially restricted to the periphery on the sarcolemma during early developmental stages and gradually appears in the cell interior as cells mature, presumably along the T-tubular membrane. This observation is indirectly supported by the similarities in the developmental time frames between NCX distribution and T-tubule development in rabbit ventricular myocytes (39). The developmental distribution changes of NCX, from peripheral restricted to cell interior dominating, reported in this study are consistent with previous reports (21,76). However, this study once again reinforces the recent finding by Dan et al. (76) that the highly organized NCX distribution is already well established in early developmental stages, contrary to earlier studies (67,74,170). Closer examination of the peripheral volume alone revealed that NCX is not distributed homogenously on the surface membrane in neonatal ventricular myocytes. We report here that NCX exists as discrete protein clusters on the cell periphery at the earliest developmental stages examined. Importantly, this surface distribution of NCX is sustained throughout development. To achieve and maintain this level of organization, the presence of underlying anchoring proteins or structural elements is highly likely.

4.1.2 Cav-3 / caveolae distribution

Caveolae and caveolin distributions in ventricular myocytes have been examined previously using electron microscopy. In freeze fracture images (171), caveolae structures appeared in clusters within 300 nm of each other. This is consistent with our findings where

cav-3 clusters appear as sub-resolved objects, approximating a point source. Freeze fracture images reveal the 3D structure and organization of caveolae on the cell membrane but do not disclose the protein constituents within the caveolae. Although cav-3 is the predominant caveolin protein expressed in ventricular myocytes, low levels of cav-1 and cav-2 protein expression have also been detected in cardiomyocytes (172,173). Therefore some of the observed caveolae detected using electron microscopy may not contain cav-3 but rather other caveolins. Available immunogold data that specifically describe the localization of cav-3 are very limited (174). In addition, the cav-3 micrographs only looked at small areas of the cell, making it difficult to visualize distribution patterns on the whole cell level. Therefore, characterization of cav-3 / caveolae on a whole cell level may prove to be difficult by electron microscopy.

4.2 Colocalization Results

Co-IP results by Bossuyt et al. (175) first suggested a direct association between NCX and cav-3 in cardiac cells. However, results from this type of analysis are highly dependent on the lipid raft isolation techniques. Two membrane solubilization methods most commonly used are based on raft resistance to high pH or non-ionic detergents. Subsequently, it was demonstrated that there are considerable differences in the protein constituents between pH/carbonate-resistant and Triton X-100-resistant fractions, with the detergent-resistant method being the more selective (176). Recently, co-fractionation and co-IP patterns of caveolin-containing fractions, prepared by these two solubilization techniques, were tested specifically (177). Using the pH/carbonate method, these authors found that all integral membrane proteins tested, including NCX, co-fractionated with cav-3. However, using the more selective detergent based method, NCX did not co-fractionate nor co-IP with cav-3 in adult rat ventricular myocytes.

Colocalization analysis from the same study showed minimal association between the two proteins but did not quantify the amount of colocalization. NCX and cav-3 colocalization were also investigated in adult rat ventricular myocytes and the authors observed 30% colocalization at the cell surface (162). In our hands, we did not find more than ~15% peripheral colocalization during rabbit ventricular development. Different species as well as different imaging methodology and parameter estimation may contribute to this variation.

As can be seen in Figure 9, both NCX and cav-3 whole cell colocalization increases during development due to increases in colocalization within the T-tubular network with no appreciable changes in peripheral colocalization. Object-specific colocalization for the

peripheral compartment (Figure 10C) did not detect a highly colocalized sub-population since the exclusion of non-colocalized objects only increased the colocalization by 5%. Despite large developmental morphological changes, the relationship between NCX and cav-3 on the peripheral compartment remained relatively constant. In each age group, object-specific analysis revealed that only ~35% of peripheral objects were associated with colocalization events. This means that the majority (~65 %) of NCX and cav-3 objects have no association with each other. Within the ~35%, the objects were only weakly colocalized at ~15%. Object-specific colocalization analysis on the interior of the cell was more difficult to interpret because developmental changes were observed both in the percentage of colocalized objects and in the colocalization percentages internal to those objects.

4.3 3D Distance Results

In this study we found the periodicity of NCX and cav-3 on the periphery of the cell ranges from 1 – 1.6 μm for both longitudinal and circumferential transverse separation distances. Not only were the ranges of the plateau phase the same, the spread of separation distances were also essentially the same. However, despite having the same periodicity, these two proteins are not highly colocalized. NCX and cav-3 clusters appear to be well separated from each other with an approximate separation distance of 0.75 – 1.25 μm. Figure 8 shows that there may be a tendency for NCX and cav-3 to alternate in both longitudinal and lateral directions. However, the underlying structural components necessary to provide this level of organization is currently undetermined.

While peripheral separations were found to be symmetrical between longitudinal and transverse events, internal events exhibited no such symmetry. The longitudinal periodicity was bimodal with a large 2 μm peak and a lesser 1 μm peak. The lesser 1 μm peak may be due to limitations in the cell peeling process, when peripheral objects were inaccurately assigned to the cell interior.

Scriven et al. reported in rat adult myocyte that cav-3 label is most likely associated with the transverse elements of the T-tubules and its interior longitudinal spacing is 1.89 μm (162), consistent with our distance measurements. The lack of a T-tubule marker in our study as well as in the Scriven et al. study makes it difficult to confirm interior cav-3 localization within the T-tubular network. However, other studies lend supporting evidence for cav-3 association with T-tubules (89). Our longitudinal periodicity data are also congruent with other groups reporting longitudinal periodicities for proteins such as RyR, $Ca_v1.2$, and ankyrin B (20,79). Very few studies have noted transverse periodicities for E-C coupling

proteins. Recently, an imaging study reported RyR transverse periodicity to be 1 μm (178), a value similar to our circumferential transverse measurement.

4.4 Physiological Implications

4.4.1 E-C Coupling Implications

We have shown unequivocally in this study that peripheral NCX distribution is sustained during development. Thus considering the decreasing contribution of NCX-mediated CICR during development, one could postulate a change in NCX-RyR proximity, as a consequence of ontogenic changes in RyR distribution. Recent immunofluorescence data from our own laboratory confirm this hypothesis by showing that RyR longitudinal periodicity changes from ~1 μm in neonatal cells to ~2 μm in adult cells (transverse periodicity is maintained at 1 μm throughout development) (179). Therefore, although cav-3 does not appear to be the structuring element for NCX-mediated CICR, other cellular proteins may still organize NCX and RyR in a functional microdomain.

The adaptor protein ankyrin B is a possible candidate responsible for the clustering and correct targeting of NCX. Recently, a direct interaction between NCX and ankyrin B was reported (180). These authors proposed a structural domain on ankyrin B that is necessary for direct NCX binding and proper NCX localization in neonatal mouse cardiomyocytes. The same group also found in another study that a heterozygous null mutation of ankyrin B (ankyrin B +/-) resulted in the abnormal localization of NCX (181). In fact, ankyrin B has been shown to affect more than just NCX localization. The loss of ankyrin B in homozygous knockout mice (ankyrin B -/-) resulted in a decrease of Na^+ current density and abnormal RyR localization (182,183). Given the apparent ability of ankyrin B to bind and organize proteins involved in E-C coupling, ankyrin B could be an important adaptor protein for NCX-CICR.

4.4.2 Other Functional Implications

Although our study focused on the functional implications of caveolae colocalization in E-C coupling, caveolae are also involved in other cellular processes including calcium homeostasis, cholesterol homeostasis, signalling transduction, and vesicular transport (111). Caveolae may exist in functionally distinct subpopulations, containing a plethora of protein constituents. It is plausible that the observed surface protein distribution of cav-3 is comprised of functionally distinct subpopulations that associate with different protein partners. Some existing colocalization data support this idea since the percentages of surface cav-3 colocalization are consistently lower by 15 - 30% than the reverse for a wide variety of proteins examined such as Na^+ channels, RyR, NCX, and $Ca_v1.2$ (162).

Similarly, NCX may also be distributed in multiple sub-populations. It was found that TRPC3 are colocalized specifically to a subpopulation of NCX found in the longitudinal component of cardiomyocyte T-tubules (184). Evidence that suggests TRPC proteins as important components of store operated channels (SOC) has been accumulating. Recently, electrophysiological data demonstrated in neonate rabbit cardiomyocytes, a significant amount of extracellular Ca^{2+} enters the cell through SOC and suggested the existence of a sarcolemmal microdomain involving SOC, SERCA2a, and NCX (185). To date, it is not clear whether subpopulations of NCX specialize in calcium extrusion while others specialize in calcium influx or whether all NCX operates in both modes. The novel analysis techniques used in this study may be useful in the delineation of protein subpopulations.

4.5 Development of New Image Processing and Analysis Techniques

4.5.1 New Thresholding Approach

Appropriate thresholding parameters are an integral part of all imaging studies, including colocalization studies between two or more proteins. Here we utilized an iterative technique in which multiple thresholds were applied to each image to obtain the number of objects per threshold value. In effect, a binary threshold (thresholding that results in a bi-level image) defines where a label is and is not located in the image. The ideal threshold is an intensity value that simultaneously minimizes false positives as well as false negatives. Under-thresholding erroneously includes dimly lit pixels from optical or labelling noise while over-thresholding can discard legitimate events. In this study we utilized the threshold value that resulted in the maximum number of events (Figure 7). At this peak location, the number of objects varied the least with changes in threshold and is a reflection of the punctate nature of both labels. It should be noted that thresholding in this manner explicitly removes diffuse fluorescence without regard to the physiological significance of that label. However, in this study high local concentrations of either label are likely to have greater physiological significance.

4.5.2 Image Segmentation Rationale

As discussed in section 1.3.1, ventricular cardiomyocytes undergo many morphological and structural changes during development. These changes make developmental comparisons difficult using traditional techniques due to the potential for multivariate changes; mainly the possibility of a variable NCX to cav-3 relationship as well

as variable membrane morphology during development. Therefore, in order to make developmental comparisons, a series of image segmentation steps were devised and applied.

First, each cell was segmented from the background image to restrict the analysis to the cell volume. Second, each cell volume was compartmentalized into peripheral and interior compartments. Thirdly, within the peripheral and interior compartments we segmented clusters of signal into individual objects that were or were not associated with colocalization events. These image segmentation steps allowed us to differentiate four possible subpopulations for each label: 1) peripheral clusters containing no colocalization events, 2) peripheral clusters containing at least one colocalization event, 3) interior clusters containing no colocalization events, and 4) interior clusters containing at least one colocalization event. These image segmentation steps revealed the nature and the source of the 10 to 15 % whole cell colocalization in each age group and made developmental comparisons possible.

4.5.3 3D over 2D Distance Analysis

An automated approach towards the measurements of separation distances between neighboring protein clusters had been previously developed (186). However, such analysis was limited to 2D images only. The 3D distance analysis approach developed for this study addresses some of the limitations traditionally associated with the 2D approach. 2D distance analysis can only report longitudinal periodicity because distances are measured from individual X-Y images instead of the entire image volume (76). Although that approach was computationally much faster than the technique used here, it also prevented the measurement of transverse periodicity. Using this newly developed 3D distance analysis technique,

calculations can be made along any arbitrary axis, and could be extended to any intermediate oblique angle if so desired.

Under Nyquist sampling conditions, a single sub-resolution object will appear in multiple image planes. Thus, when making 2D periodicity measurements, there is no guarantee that a pair of objects will not be used for redundant calculations in multiple image planes. Furthermore, using individual XY slices for distance analysis limits distance calculations to where the probability of axial resolution interferences is the greatest. Our 3D approach reduced each cluster event to a single XYZ co-ordinate. This conversion limits redundant distances as well as the effects of z-resolution interference.

Although there are distinct advantages associated with this 3D distance analysis, this technique is not without limitations. This technique is computationally more expensive than our 2D analysis and accurate distance calculations are contingent on obtaining an accurate cell outline. However, the 3D approach utilizes more of the image area and batch processing has largely limited the need for user interaction.

4.5.4 Application of New Imaging Techniques

Our newly developed analysis technique can have wide applicability across many areas of cell biology research such as lipid raft research. Many studies have advanced our understanding of membrane lipid and protein interactions since the inception of the lipid raft field; however, unequivocal evidence is still needed to address controversies regarding the existence, turnover rate, size, and function of lipid rafts. The most notable technical impasse is the inability to visualize lipid rafts other than caveolae. Refinement of existing imaging tools and development of new detection methods for raft visualization are currently underway. Coupled with our technique, spatial relationships between functionally or

biochemically distinct lipid rafts and between lipid rafts and other cellular structures can then be better characterized.

4.6 Experimental Limitations

4.6.1 Immunolabeling Considerations

Since we are studying the spatial relationship between two integral membrane proteins, preservation of the membrane integrity was critically important in this study. However, membrane structures may be compromised during the cell permeabilization process necessary for antibody penetration. The labelling protocol used in this study has been optimized to achieve the highest possible image quality. Multiple combinations of the incubation times, labelling order, and antibody concentrations were tested to maximize the signal-to-noise ratio. Meanwhile, the concentrations and exposure times of triton X-100, the permeabilizing agent, and paraformaldehyde, the fixative of choice, were minimized to prevent antigen extraction and excessive cross-linking.

Specificity of primary antibody is usually determined by blocking experiments using the epitope peptides. These experiments were not done in this particular study, but the specificities of these two antibodies have been firmly established in previous studies (187,188). Specificity of secondary antibody established in control experiments where either control primary antibodies or isotype mismatched primary antibodies were used. The robust alternating pattern of distribution for these two labels suggests antibody accessibility competition was not the reason for the lack of colocalization. If spatial competition between the two antibodies were responsible for the low colocalization, no alternating pattern of distribution should be observed since antibody competition at each antigen site should be

independent and random, if the binding affinities of each antibody to the respective antigen were on the same order of magnitude. In contrast, if the binding affinity between one antibody-antigen complex is significantly higher, one would expect to see a labelling pattern for that complex to be dominant. Neither scenario is observed in the actual data set; in addition, the sequence of antibody application was reversed or changed to simultaneous in one set of control experiments and no distribution changes were observed. Thus I conclude that the low colocalization observed in this study is not a result of antibody accessibility issues.

4.6.2 Limitations of Confocal Microscopy

4.6.2.1 Resolution Limit

The most apparent shortcoming with the use of a light microscope in colocalization studies is the resolution limit. Even with deconvolution, the lateral resolution limit of a confocal microscope is around 300 nm and the axial resolution limit is around 500 nm (189). These distances are significantly larger than the resolving power of electron microscopes at less than 10 nm. In E-C coupling, spatial proximity between two proteins is critically important for functional coupling. It has been suggested that two proteins should be within 20 nm of each other in order for functional coupling to occur (1). Unfortunately, any studies utilizing light microscopes for the determination of protein colocalization can only suggest spatial proximity at the level of the resolution limit of the system, but fails to extend such findings to imply functional coupling between the colocalized proteins.

4.6.2.2 Imaging Artifacts

In any imaging system, there exists the possibility for the introduction of imaging artifacts. For example, in our analysis, colocalization events were not found to be homogeneously distributed along the circumference of the cell. Figure 12A shows a representative cell-surface image compiled from the surface layer of the cell outline. The number of colocalization events per vertical column of the cell-surface image is shown in Figure 12B. Colocalization events were found to appear more often on lateral aspects of the cell (positions 1, 3 and 5 in figure 12C, D) and less often in areas corresponding to the top and bottom surfaces of the cell (positions 2 and 4 in Figures 12C, D).

The higher lateral colocalization may be related to the axial and lateral resolutions of the confocal microscope. Our distance analyses found transverse spacing of both NCX and cav-3 to be comparable to the limits of our axial resolution at around 1 μm. Therefore, it appears that objects along the sides of the cell, where z-resolution limited effects are greatest, are blurred together during the imaging process, thereby causing pseudo-colocalization between the two proteins. This colocalization heterogeneity may be worth further consideration in subsequent studies.

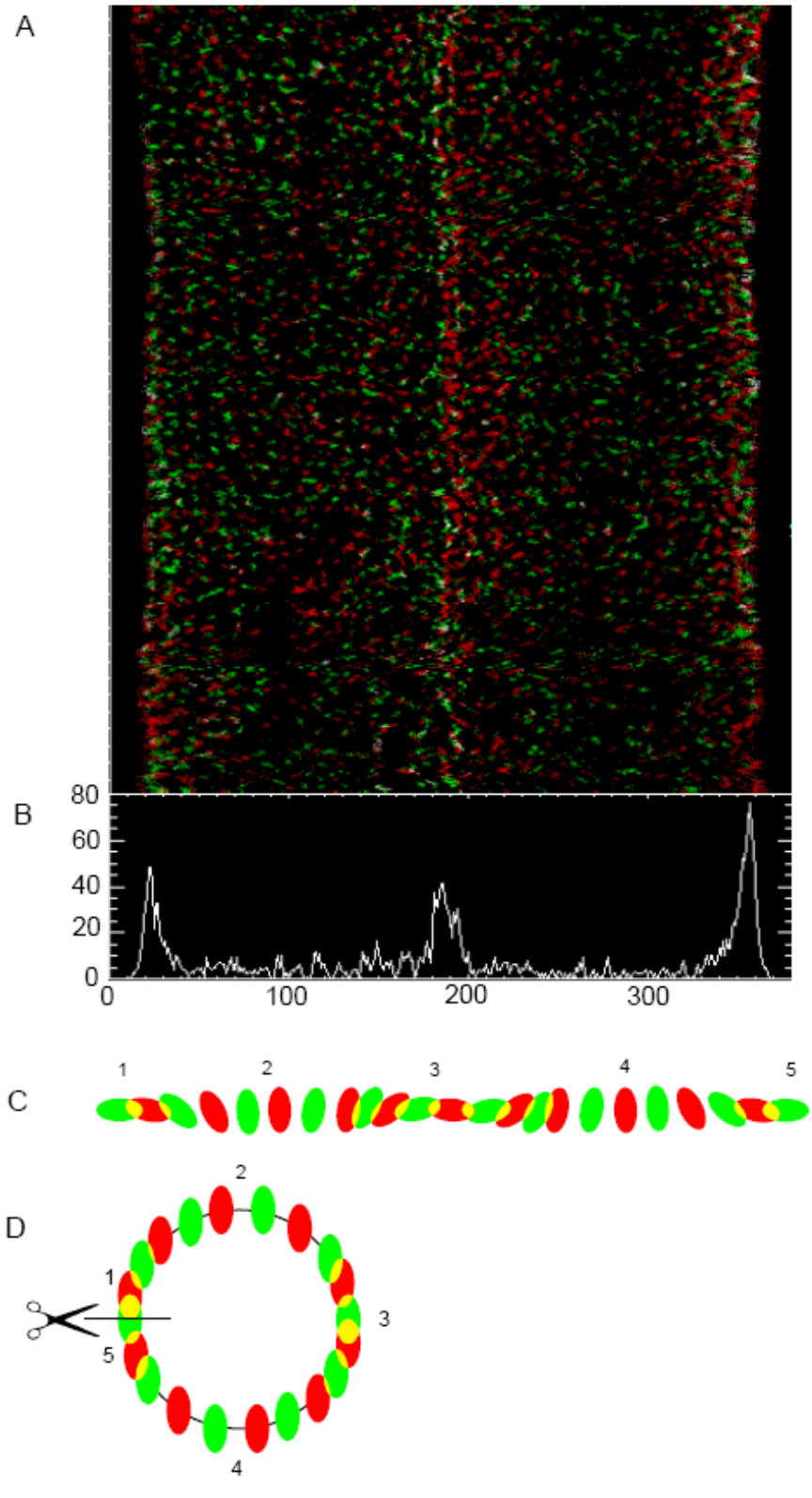
A
B
80
60
40
20
0
0
100
200
300
C
1
2
3
4
5
D
1
2
3
4
5

Figure 12: Resolution dependent colocalization distribution profile.
(A) is an image of the cell surface volume compiled from the 3D co-ordinates of the cell surface fluorescence clusters. (B) is the corresponding histogram showing the number of colocalized events (y-axis) relative to the cell circumference (x-axis). (C) and (D) show diagrammatically how the image of the cell surface was generated. The cell surface was cut along the left edge and then unravelled. Red represents NCX label, green represents cav-3 label, and colocalized voxels are displayed in white. (A) and (B) clearly demonstrate how the distribution of colocalized voxels is not uniform across the cell circumference. Rather, colocalized voxels appear more often at positions 1, 3, and 5 where the large axial resolution limit may render neighbouring fluorescence clusters non-resolvable, ultimately resulting in pseudo-colocalization.

4.6.2.3 Photobleaching

The phenomenon of photobleaching occurs when a fluorophore permanently loses its ability to fluoresce due to photon-induced chemical damage and covalent modification. During excitation state transition, fluorophores may interact with another molecule such as oxygen to produce irreversible covalent modifications. Destruction of the fluorophores results in the fading of the specimen. Regardless of the illumination source, photobleaching is an applicable concern in imaging studies. Both wide-field and laser scanning confocal microscopy (LSCM) face the challenging task of maximizing signal while minimizing photo-damage to specimen. However, since laser is a higher intensity light source over white light used in wide-field fluorescent microscopy, the damage induced by a LSCM system is also conceivably more significant.

4.6.2.4 Sensitivity vs. Specificity

The most distinctive advantage a confocal microscope offers over traditional wide-field fluorescence microscope is the capability to collect serial optical sections from thick specimens. In a conventional wide-field epi-fluorescence microscope, the illumination source is often an arc lamp that will excite fluorophores lying outside of the objective focal plane. This out-of-focus fluorescence emission results in the obscuring of the resultant image. Confocal microscopy provides only a marginal improvement in both axial and lateral optical resolution, but is able to exclude secondary fluorescence. This is primarily achieved by the introduction of a pinhole that eliminates out-of-focus light or glare in specimens whose thickness exceeds the dimensions of the focal plane. The pinhole increases image resolution at the cost of reducing the amount of light detected. The lower photon count, in turn results in longer acquisition times which further exacerbate the photobleaching problem.

It is well known that the absolute numbers of photons collected in a confocal system are less than that in a wide-field imaging system. However, images collected by a confocal imaging system also generally have higher signal to noise ratios. Hence, LSCM can be considered as a more specific but less sensitive method than wide-field fluorescence microscopy. Swedlow et al. (190) demonstrated how weakly fluorescent structures below the detection limit of a LSCM system was successfully imaged by wide-field microscopy. Thus, the possibility exists that some dimly lit diffuse label in our cells may be below the sensitivity limit of our imaging system. However, since the focus of this study was to specifically analyze the spatial organization of high density protein clusters, this limitation of LSCM is of less consequence to the interpretation of the data.

4.6.2.5 Two-photon v.s. Conventional Confocal Microscopy

A recently developed confocal microscopy technique, the two-photon laser scanning microscope, has certain advantages over traditional laser scanning confocal microscopy. In brief, the main differences between the two techniques are the wavelength and the illumination time of the excitation laser used. In two-photon microscopy, the focal plane is illuminated with high intensity light at twice the excitation wavelength of the target fluorophores. Since a longer wavelength is used, fluorophores require two sequential hits from the excitation beam to raise electrons to an elevated state thus emitting fluorescence. The high intensity illumination, attained by focusing a beam from a high energy pulsed laser at high frequencies, enables the arrival of two photons separated only by several femtoseconds. Images are built up by scanning the laser illumination across the specimen and changing the focal plane, as with the conventional confocal laser-scanning microscope.

In this way, optical sectioning is obtained intrinsically by the two photon effect, rather than by the use of pinholes in a conventional confocal laser-scanning microscope.

The major advantages two-photon microscopy offers are: 1) non-linear excitation, and 2) higher penetrance. The requirement for two coincident (or near coincident) photons to achieve excitation of the fluorophore means that only focused light reaches the required intensities and that scattered light does not cause excitation of the fluorophore. Thus, the design of the two-photon laser scanning microscope makes it inherently insensitive to the effects of light scattering in thick slices, which are normally quite detrimental to the contrast of the final images. On the other hand, the higher penetrance is partly due to the use of longer red and near-infrared wavelengths. As a consequence of the inherent property of light waves, longer wavelengths can penetrate deeper into biological tissue with less absorption and scattering.

These properties make two-photon microscopy particularly useful when working with thick tissues, such as brain slices or developing embryos. However, the thickness of the myocytes (5-15 μm) used in the present study does not warrant the use of a two-photon microscope, which is significantly more expensive than a conventional confocal microscope.

CHAPTER V: CONCLUSIONS

The phenotypic differences in E-C coupling between the adult and neonatal cardiac systems result in their differential responses to physiological, pathological and pharmacological perturbations. To ensure favourable outcomes after surgical or pharmacological interventions for the pediatric population, detailed knowledge of the E-C coupling mechanisms in the neonatal heart and how it changes with development is indispensable.

The overall objective of this study was to investigate the developmental changes in the spatial organization / relationship of two integral membrane proteins implicated in E-C coupling, NCX and cav-3. Previous morphological, biochemical, as well as functional data suggest an association between these two proteins. Other experiments have implicated the existence of a restricted microdomain particularly in neonatal cells and one such microdomain can facilitate the process of CICR in neonatal cells.

As cav-3 is the principle structural protein of caveolae, we proposed that caveolae are the structural microdomain responsible for organizing NCX into high density protein clusters positioned in close proximity to RyR in rabbit neonatal ventricular myocytes. We further hypothesize that this spatial organization undergoes extensive changes during development such that the colocalization between two proteins gradually declines and reaches minimal levels in adult cells. Our major findings are:

1) in rabbit ventricular myocytes, peripheral NCX and cav-3 distribution pattern did not change during development
2) both NCX and cav-3 exist as punctate clusters on the periphery in all age groups examined

3) NCX and cav-3 are minimally colocalized at < 15%; no major changes in colocalization percentages were observed during development

4) the peripheral transverse and longitudinal separation distances range from 1 – 1.6 μm for both NCX and cav-3

5) NCX to cav-3 separation on the periphery is consistently less than that between two NCX clusters or two cav-3 clusters ranging from 0.75 – 1.25 μm

6) both qualitative and quantitative analysis suggest NCX and cav-3 protein clusters alternate along the periphery of the cell both longitudinally and transversely

7) both NCX and cav-3 appear in the interior of the cell as T-tubules develop, presumably located along the T-tubular membrane

8) in more developed cells with T-tubules (20 day old and 56 day old), internal transverse periodicities are around 1 μm and longitudinal periodicities are near 2 μm for both NCX and cav-3

The colocalization results do not support our original hypothesis. This implies that caveolae may not be the structural microdomain facilitating NCX-mediated CICR in rabbit neonatal ventricular myocytes. However, results from this study do not exclude the possibility that other anchoring proteins may provide the structural basis for NCX-containing restricted microdomains. Other qualitative and quantitative findings from this study firmly establish the highly robust and organized nature of the protein distributions of NCX and cav-3 during development. In addition, the novel image processing and analysis techniques developed during this project can have wide applicability to other imaging studies.

REFERENCES

1. Tibbits, G. F., L. Xu, F. Sedarat. 2002. Ontogeny of excitation-contraction coupling in the mammalian heart. Comp Biochem Physiol A Mol Integr Physiol. 132(4):691-698.
2. Jacobs, J. P., C. Mavroudis, M. L. Jacobs, F. G. Lacour-Gayet, C. I. Tchervenkov, J. William Gaynor, D. R. Clarke, T. L. Spray, B. Maruszewski, G. Stellin and others. 2004. Lessons learned from the data analysis of the second harvest (1998-2001) of the Society of Thoracic Surgeons (STS) Congenital Heart Surgery Database. Eur J Cardiothorac Surg. 26(1):18-37.
3. Mildh, L., V. Pettila, H. Sairanen, P. Rautiainen. 2007. Predictive value of pediatric risk of mortality score and risk adjustment for congenital heart surgery score after pediatric open-heart surgery. Interact Cardiovasc Thorac Surg.
4. Tu, J. V., C. D. Naylor. 1996. Coronary artery bypass mortality rates in Ontario. A Canadian approach to quality assurance in cardiac surgery. Steering Committee of the Provincial Adult Cardiac Care Network of Ontario. Circulation. 94(10):2429-2433.
5. Fabiato, A. 1983. Calcium-induced release of calcium from the cardiac sarcoplasmic reticulum. Am J Physiol. 245(1):C1-14.
6. Bers, D. M. 2001. Excitation–Contraction Coupling and Cardiac Contractile Force. Dordrecht, Netherlands: Kluwer Academic. 427 p.
7. Bers, D. M. 2002. Cardiac excitation-contraction coupling. Nature. 415(6868):198-205.
8. Wier, W. G., T. M. Egan, J. R. Lopez-Lopez, C. W. Balke. 1994. Local control of excitation-contraction coupling in rat heart cells. J Physiol. 474(3):463-471.
9. Shannon, T. R., K. S. Ginsburg, D. M. Bers. 2000. Potentiation of fractional sarcoplasmic reticulum calcium release by total and free intra-sarcoplasmic reticulum calcium concentration. Biophys J. 78(1):334-343.
10. Luo, C. H., Y. Rudy. 1994. A dynamic model of the cardiac ventricular action potential. I. Simulations of ionic currents and concentration changes. Circ Res. 74(6):1071-1096.
11. Hilgemann, D. W., D. Noble. 1987. Excitation-contraction coupling and extracellular calcium transients in rabbit atrium: reconstruction of basic cellular mechanisms. Proc R Soc Lond B Biol Sci. 230(1259):163-205.
12. Noble, D., A. Varghese, P. Kohl, P. Noble. 1998. Improved guinea-pig ventricular cell model incorporating a diadic space, IKr and IKs, and length- and tension-dependent processes. Can J Cardiol. 14(1):123-134.
13. Winslow, R. L., J. Rice, S. Jafri, E. Marban, B. O'Rourke. 1999. Mechanisms of altered excitation-contraction coupling in canine tachycardia-induced heart failure, II: model studies. Circ Res. 84(5):571-586.
14. Fabiato, A. 1985. Rapid ionic modifications during the aequorin-detected calcium transient in a skinned canine cardiac Purkinje cell. J Gen Physiol. 85(2):189-246.
15. Fabiato, A. 1985. Simulated calcium current can both cause calcium loading in and trigger calcium release from the sarcoplasmic reticulum of a skinned canine cardiac Purkinje cell. J Gen Physiol. 85(2):291-320.
16. Fabiato, A. 1985. Time and calcium dependence of activation and inactivation of calcium-induced release of calcium from the sarcoplasmic reticulum of a skinned canine cardiac Purkinje cell. J Gen Physiol. 85(2):247-289.

17. Sham, J. S. 1997. Ca2+ release-induced inactivation of Ca2+ current in rat ventricular myocytes: evidence for local Ca2+ signalling. J Physiol. 500 (Pt 2):285-295.
18. Stern, M. D. 1992. Theory of excitation-contraction coupling in cardiac muscle. Biophys J. 63(2):497-517.
19. Frank, J. S., G. Mottino, D. Reid, R. S. Molday, K. D. Philipson. 1992. Distribution of the Na^+-Ca^{2+} exchange protein in mammalian cardiac myocytes: an immunofluorescence and immunocolloidal gold-labeling study. J Cell Biol. 117(2):337-345.
20. Scriven, D. R., P. Dan, E. D. Moore. 2000. Distribution of proteins implicated in excitation-contraction coupling in rat ventricular myocytes. Biophys J. 79(5):2682-2691.
21. Chen, F., G. Mottino, T. S. Klitzner, K. D. Philipson, J. S. Frank. 1995. Distribution of the Na+/Ca2+ exchange protein in developing rabbit myocytes. Am J Physiol. 268(5 Pt 1):C1126-1132.
22. Maier, S. K., R. E. Westenbroek, K. A. McCormick, R. Curtis, T. Scheuer, W. A. Catterall. 2004. Distinct subcellular localization of different sodium channel alpha and beta subunits in single ventricular myocytes from mouse heart. Circulation. 109(11):1421-1427.
23. Maier, S. K., R. E. Westenbroek, K. A. Schenkman, E. O. Feigl, T. Scheuer, W. A. Catterall. 2002. An unexpected role for brain-type sodium channels in coupling of cell surface depolarization to contraction in the heart. Proc Natl Acad Sci U S A. 99(6):4073-4078.
24. Carl, S. L., K. Felix, A. H. Caswell, N. R. Brandt, W. J. Ball, Jr., P. L. Vaghy, G. Meissner, D. G. Ferguson. 1995. Immunolocalization of sarcolemmal dihydropyridine receptor and sarcoplasmic reticular triadin and ryanodine receptor in rabbit ventricle and atrium. J Cell Biol. 129(3):672-682.
25. Ogata, T., Y. Yamasaki. 1990. High-resolution scanning electron microscopic studies on the three-dimensional structure of the transverse-axial tubular system, sarcoplasmic reticulum and intercalated disc of the rat myocardium. Anat Rec. 228(3):277-287.
26. Sun, X. H., F. Protasi, M. Takahashi, H. Takeshima, D. G. Ferguson, C. Franzini-Armstrong. 1995. Molecular architecture of membranes involved in excitation-contraction coupling of cardiac muscle. J Cell Biol. 129(3):659-671.
27. Nicoll, D. A., M. Ottolia, L. Lu, Y. Lu, K. D. Philipson. 1999. A new topological model of the cardiac sarcolemmal Na^+-Ca^{2+} exchanger. J Biol Chem. 274(2):910-917.
28. Nicoll, D. A., S. Longoni, K. D. Philipson. 1990. Molecular cloning and functional expression of the cardiac sarcolemmal Na^+/$Ca2^+$ exchanger. Science. 250(4980):562-565.
29. Nicoll, D. A., X. Ren, M. Ottolia, M. Phillips, A. R. Paredes, J. Abramson, K. D. Philipson. 2007. What we know about the structure of NCX1 and how it relates to its function. Ann N Y Acad Sci. 1099:1-6.
30. Lytton, J. 2007. Na+/Ca2+ exchangers: three mammalian gene families control Ca2+ transport. Biochem J. 406(3):365-382.
31. Reeves, J. P., C. C. Hale. 1984. The stoichiometry of the cardiac sodium-calcium exchange system. J Biol Chem. 259(12):7733-7739.
32. Hilgemann, D. W., A. Collins, S. Matsuoka. 1992. Steady-state and dynamic properties of cardiac sodium-calcium exchange. Secondary modulation by cytoplasmic calcium and ATP. J Gen Physiol. 100(6):933-961.
33. Bers, D. M., W. H. Barry, S. Despa. 2003. Intracellular Na+ regulation in cardiac myocytes. Cardiovasc Res. 57(4):897-912.

34. Despa, S., M. A. Islam, C. R. Weber, S. M. Pogwizd, D. M. Bers. 2002. Intracellular Na^+ concentration is elevated in heart failure but Na^+/K^+ pump function is unchanged. Circulation. 105(21):2543-2548.
35. Nuss, H. B., S. R. Houser. 1992. Sodium-calcium exchange-mediated contractions in feline ventricular myocytes. Am J Physiol. 263(4 Pt 2):H1161-1169.
36. Despa, S., M. A. Islam, C. R. Weber, S. M. Pogwizd, D. M. Bers. 2002. Intracellular Na(+) concentration is elevated in heart failure but Na/K pump function is unchanged. Circulation. 105(21):2543-2548.
37. Pott, C., S. A. Henderson, J. I. Goldhaber, K. D. Philipson. 2007. Na+/Ca2+ exchanger knockout mice: plasticity of cardiac excitation-contraction coupling. Ann N Y Acad Sci. 1099:270-275.
38. Sarai, N., T. Kobayashi, S. Matsuoka, A. Noma. 2006. A simulation study to rescue the Na+/Ca2+ exchanger knockout mice. J Physiol Sci. 56(3):211-217.
39. Hoerter, J., F. Mazet, G. Vassort. 1981. Perinatal growth of the rabbit cardiac cell: possible implications for the mechanism of relaxation. J Mol Cell Cardiol. 13(8):725-740.
40. Huang, J., L. Hove-Madsen, G. F. Tibbits. 2005. Na+/Ca2+ exchange activity in neonatal rabbit ventricular myocytes. Am J Physiol Cell Physiol. 288(1):C195-203.
41. Legato, M. J. 1979. Cellular mechanisms of normal growth in the mammalian heart. II. A quantitative and qualitative comparison between the right and left ventricular myocytes in the dog from birth to five months of age. Circ Res. 44(2):263-279.
42. Nassar, R., M. C. Reedy, P. A. Anderson. 1987. Developmental changes in the ultrastructure and sarcomere shortening of the isolated rabbit ventricular myocyte. Circ Res. 61(3):465-483.
43. Satoh, H., L. M. Delbridge, L. A. Blatter, D. M. Bers. 1996. Surface:volume relationship in cardiac myocytes studied with confocal microscopy and membrane capacitance measurements: species-dependence and developmental effects. Biophys J. 70(3):1494-1504.
44. Soeller, C., M. B. Cannell. 1999. Examination of the transverse tubular system in living cardiac rat myocytes by 2-photon microscopy and digital image-processing techniques. Circ Res. 84(3):266-275.
45. Brette, F., C. Orchard. 2003. T-tubule function in mammalian cardiac myocytes. Circ Res. 92(11):1182-1192.
46. Page, E., J. L. Buecker. 1981. Development of dyadic junctional complexes between sarcoplasmic reticulum and plasmalemma in rabbit left ventricular myocardial cells. Morphometric analysis. Circ Res. 48(4):519-522.
47. Pegg, W., M. Michalak. 1987. Differentiation of sarcoplasmic reticulum during cardiac myogenesis. Am J Physiol. 252(1 Pt 2):H22-31.
48. Forsgren, S., L. E. Thornell. 1981. The development of Purkinje fibres and ordinary myocytes in the bovine fetal heart. An ultrastructural study. Anat Embryol (Berl). 162(2):127-136.
49. Nowycky, M. C., A. P. Fox, R. W. Tsien. 1985. Three types of neuronal calcium channel with different calcium agonist sensitivity. Nature. 316(6027):440-443.
50. Jurkat-Rott, K., F. Lehmann-Horn. 2004. The impact of splice isoforms on voltage-gated calcium channel alpha1 subunits. J Physiol. 554(Pt 3):609-619.
51. Ertel, E. A., K. P. Campbell, M. M. Harpold, F. Hofmann, Y. Mori, E. Perez-Reyes, A. Schwartz, T. P. Snutch, T. Tanabe, L. Birnbaumer and others. 2000. Nomenclature of voltage-gated calcium channels. Neuron. 25(3):533-535.

52. Huang, J., L. Xu, M. Thomas, K. Whitaker, L. Hove-Madsen, G. F. Tibbits. 2006. L-type Ca^{2+} channel function and expression in neonatal rabbit ventricular myocytes. Am J Physiol Heart Circ Physiol. 290(6):H2267-2276.
53. Haufe, V., J. A. Camacho, R. Dumaine, B. Gunther, C. Bollensdorff, G. S. von Banchet, K. Benndorf, T. Zimmer. 2005. Expression pattern of neuronal and skeletal muscle voltage-gated Na+ channels in the developing mouse heart. J Physiol. 564(Pt 3):683-696.
54. Brandl, C. J., S. deLeon, D. R. Martin, D. H. MacLennan. 1987. Adult forms of the Ca2+ATPase of sarcoplasmic reticulum. Expression in developing skeletal muscle. J Biol Chem. 262(8):3768-3774.
55. Brandl, C. J., N. M. Green, B. Korczak, D. H. MacLennan. 1986. Two Ca2+ ATPase genes: homologies and mechanistic implications of deduced amino acid sequences. Cell. 44(4):597-607.
56. Gunteski-Hamblin, A. M., J. Greeb, G. E. Shull. 1988. A novel Ca2+ pump expressed in brain, kidney, and stomach is encoded by an alternative transcript of the slow-twitch muscle sarcoplasmic reticulum Ca-ATPase gene. Identification of cDNAs encoding Ca2+ and other cation-transporting ATPases using an oligonucleotide probe derived from the ATP-binding site. J Biol Chem. 263(29):15032-15040.
57. MacLennan, D. H., C. J. Brandl, B. Korczak, N. M. Green. 1985. Amino-acid sequence of a Ca2+ + Mg2+-dependent ATPase from rabbit muscle sarcoplasmic reticulum, deduced from its complementary DNA sequence. Nature. 316(6030):696-700.
58. Wu, K. D., J. Lytton. 1993. Molecular cloning and quantification of sarcoplasmic reticulum Ca(2+)-ATPase isoforms in rat muscles. Am J Physiol. 264(2 Pt 1):C333-341.
59. Wuytack, F., B. Papp, H. Verboomen, L. Raeymaekers, L. Dode, R. Bobe, J. Enouf, S. Bokkala, K. S. Authi, R. Casteels. 1994. A sarco/endoplasmic reticulum Ca(2+)-ATPase 3-type Ca2+ pump is expressed in platelets, in lymphoid cells, and in mast cells. J Biol Chem. 269(2):1410-1416.
60. Campbell, A. M., P. D. Kessler, D. M. Fambrough. 1992. The alternative carboxyl termini of avian cardiac and brain sarcoplasmic reticulum/endoplasmic reticulum Ca(2+)-ATPases are on opposite sides of the membrane. J Biol Chem. 267(13):9321-9325.
61. Mercadier, J. J., A. M. Lompre, P. Duc, K. R. Boheler, J. B. Fraysse, C. Wisnewsky, P. D. Allen, M. Komajda, K. Schwartz. 1990. Altered sarcoplasmic reticulum Ca^{2+}-ATPase gene expression in the human ventricle during end-stage heart failure. J Clin Invest. 85(1):305-309.
62. Fisher, D. J., C. A. Tate, S. Phillips. 1992. Developmental regulation of the sarcoplasmic reticulum calcium pump in the rabbit heart. Pediatr Res. 31(5):474-479.
63. Harrer, J. M., K. Haghighi, H. W. Kim, D. G. Ferguson, E. G. Kranias. 1997. Coordinate regulation of SR Ca^{2+}-ATPase and phospholamban expression in developing murine heart. Am J Physiol. 272(1 Pt 2):H57-66.
64. Boerth, S. R., D. B. Zimmer, M. Artman. 1994. Steady-state mRNA levels of the sarcolemmal Na^{+}-Ca^{2+} exchanger peak near birth in developing rabbit and rat hearts. Circ Res. 74(2):354-359.
65. Artman, M., H. Ichikawa, M. Avkiran, W. A. Coetzee. 1995. Na^{+}-Ca^{2+} exchange current density in cardiac myocytes from rabbits and guinea pigs during postnatal development. Am J Physiol. 268(4 Pt 2):H1714-1722.
66. Haddock, P. S., W. A. Coetzee, M. Artman. 1997. Na^{+}/Ca^{2+} exchange current and contractions measured under Cl^{-}-free conditions in developing rabbit hearts. Am J Physiol. 273(2 Pt 2):H837-846.

67. Wetzel, G. T., F. Chen, T. S. Klitzner. 1995. Na^+/Ca^{2+} exchange and cell contraction in isolated neonatal and adult rabbit cardiac myocytes. Am J Physiol. 268(4 Pt 2):H1723-1733.
68. London, B., J. W. Krueger. 1986. Contraction in voltage-clamped, internally perfused single heart cells. J Gen Physiol. 88(4):475-505.
69. Terracciano, C. M., K. T. MacLeod. 1994. Effects of acidosis on Na^+/Ca^{2+} exchange and consequences for relaxation in guinea pig cardiac myocytes. Am J Physiol. 267(2 Pt 2):H477-487.
70. Delbridge, L. M., J. W. Bassani, D. M. Bers. 1996. Steady-state twitch Ca^{2+} fluxes and cytosolic Ca^{2+} buffering in rabbit ventricular myocytes. Am J Physiol. 270(1 Pt 1):C192-199.
71. Pieske, B., L. S. Maier, D. M. Bers, G. Hasenfuss. 1999. Ca^{2+} handling and sarcoplasmic reticulum Ca^{2+} content in isolated failing and nonfailing human myocardium. Circ Res. 85(1):38-46.
72. Kohomoto, O., A. J. Levi, J. H. Bridge. 1994. Relation between reverse sodium-calcium exchange and sarcoplasmic reticulum calcium release in guinea pig ventricular cells. Circ Res. 74(3):550-554.
73. Litwin, S. E., J. Li, J. H. Bridge. 1998. Na^+-Ca^{2+} exchange and the trigger for sarcoplasmic reticulum Ca^{2+} release: studies in adult rabbit ventricular myocytes. Biophys J. 75(1):359-371.
74. Haddock, P. S., W. A. Coetzee, E. Cho, L. Porter, H. Katoh, D. M. Bers, M. S. Jafri, M. Artman. 1999. Subcellular [Ca2+]i gradients during excitation-contraction coupling in newborn rabbit ventricular myocytes. Circ Res. 85(5):415-427.
75. Seki, S., M. Nagashima, Y. Yamada, M. Tsutsuura, T. Kobayashi, A. Namiki, N. Tohse. 2003. Fetal and postnatal development of Ca^{2+} transients and Ca^{2+} sparks in rat cardiomyocytes. Cardiovasc Res. 58(3):535-548.
76. Dan, P., E. Lin, J. Huang, P. Biln, G. F. Tibbits. 2007. Three-dimensional distribution of cardiac Na+-Ca2+ exchanger and ryanodine receptor during development. Biophys J. 93(7):2504-2518.
77. Hilgemann, D. W., A. Collins, D. P. Cash, G. A. Nagel. 1991. Cardiac Na^+-Ca^{2+} exchange system in giant membrane patches. Ann N Y Acad Sci. 639:126-139.
78. Sedarat, F., L. Xu, E. D. Moore, G. F. Tibbits. 2000. Colocalization of dihydropyridine and ryanodine receptors in neonate rabbit heart using confocal microscopy. Am J Physiol Heart Circ Physiol. 279(1):H202-209.
79. Chen, F., G. Mottino, V. Y. Shin, J. S. Frank. 1997. Subcellular distribution of ankyrin in developing rabbit heart--relationship to the Na^+-Ca^{2+} exchanger. J Mol Cell Cardiol. 29(10):2621-2629.
80. Sedarat, F., E. Lin, E. D. Moore, G. F. Tibbits. 2004. Deconvolution of Confocal Images of Dihydropyridine and Ryanodine Receptors in Developing Cardiomyocytes. J Appl Physiol.
81. Silverman, B. Z., A. Warley, J. I. Miller, A. F. James, M. J. Shattock. 2003. Is there a transient rise in sub-sarcolemmal Na^+ and activation of Na^+/K^+ pump current following activation of I_{Na} in ventricular myocardium? Cardiovasc Res. 57(4):1025-1034.
82. Trafford, A. W., M. E. Diaz, S. C. O'Neill, D. A. Eisner. 1995. Comparison of subsarcolemmal and bulk calcium concentration during spontaneous calcium release in rat ventricular myocytes. J Physiol. 488 (Pt 3):577-586.
83. Weber, C. R., V. Piacentino, 3rd, K. S. Ginsburg, S. R. Houser, D. M. Bers. 2002. Na^+-Ca^{2+} exchange current and submembrane $[Ca^{2+}]$ during the cardiac action potential. Circ Res. 90(2):182-189.

84. Stern, M. D. 1992. Buffering of calcium in the vicinity of a channel pore. Cell Calcium. 13(3):183-192.
85. Leblanc, N., J. R. Hume. 1990. Sodium current-induced release of calcium from cardiac sarcoplasmic reticulum. Science. 248(4953):372-376.
86. Poburko, D., C. H. Liao, V. S. Lemos, E. Lin, Y. Maruyama, W. C. Cole, C. van Breemen. 2007. Transient receptor potential channel 6-mediated, localized cytosolic [Na+] transients drive Na+/Ca2+ exchanger-mediated Ca2+ entry in purinergically stimulated aorta smooth muscle cells. Circ Res. 101(10):1030-1038.
87. Palade, G. E. 1953. An electron microscope study of the mitochondrial structure. J Histochem Cytochem. 1(4):188-211.
88. Yamada, E. 1955. The fine structure of the gall bladder epithelium of the mouse. J Biophys Biochem Cytol. 1(5):445-458.
89. Parton, R. G., M. Way, N. Zorzi, E. Stang. 1997. Caveolin-3 associates with developing T-tubules during muscle differentiation. J Cell Biol. 136(1):137-154.
90. Simionescu, N., M. Siminoescu, G. E. Palade. 1975. Permeability of muscle capillaries to small heme-peptides. Evidence for the existence of patent transendothelial channels. J Cell Biol. 64(3):586-607.
91. Karnovsky, M. J., A. M. Kleinfeld, R. L. Hoover, R. D. Klausner. 1982. The concept of lipid domains in membranes. J Cell Biol. 94(1):1-6.
92. Thompson, T. E., T. W. Tillack. 1985. Organization of glycosphingolipids in bilayers and plasma membranes of mammalian cells. Annu Rev Biophys Biophys Chem. 14:361-386.
93. Hooper, N. M., A. J. Turner. 1988. Ectoenzymes of the kidney microvillar membrane. Differential solubilization by detergents can predict a glycosyl-phosphatidylinositol membrane anchor. Biochem J. 250(3):865-869.
94. Brown, D. A., J. K. Rose. 1992. Sorting of GPI-anchored proteins to glycolipid-enriched membrane subdomains during transport to the apical cell surface. Cell. 68(3):533-544.
95. Brown, D. A., E. London. 1998. Structure and origin of ordered lipid domains in biological membranes. J Membr Biol. 164(2):103-114.
96. Simons, K., D. Toomre. 2000. Lipid rafts and signal transduction. Nat Rev Mol Cell Biol. 1(1):31-39.
97. Galbiati, F., B. Razani, M. P. Lisanti. 2001. Caveolae and caveolin-3 in muscular dystrophy. Trends Mol Med. 7(10):435-441.
98. Gabella, G. 1978. Inpocketings of the cell membrane (caveolae) in the rat myocardium. J Ultrastruct Res. 65(2):135-147.
99. Gil, J. 1983. Number and distribution of plasmalemmal vesicles in the lung. Fed Proc. 42(8):2414-2418.
100. Mobley, B. A., B. R. Eisenberg. 1975. Sizes of components in frog skeletal muscle measured by methods of stereology. J Gen Physiol. 66(1):31-45.
101. Napolitano, L. 1963. The Differentiation of White Adipose Cells. an Electron Microscope Study. J Cell Biol. 18:663-679.
102. Glenney, J. R., Jr., L. Zokas. 1989. Novel tyrosine kinase substrates from Rous sarcoma virus-transformed cells are present in the membrane skeleton. J Cell Biol. 108(6):2401-2408.
103. Rothberg, K. G., J. E. Heuser, W. C. Donzell, Y. S. Ying, J. R. Glenney, R. G. Anderson. 1992. Caveolin, a protein component of caveolae membrane coats. Cell. 68(4):673-682.

104. Scherer, P. E., T. Okamoto, M. Chun, I. Nishimoto, H. F. Lodish, M. P. Lisanti. 1996. Identification, sequence, and expression of caveolin-2 defines a caveolin gene family. Proc Natl Acad Sci U S A. 93(1):131-135.
105. Tang, Z., P. E. Scherer, T. Okamoto, K. Song, C. Chu, D. S. Kohtz, I. Nishimoto, H. F. Lodish, M. P. Lisanti. 1996. Molecular cloning of caveolin-3, a novel member of the caveolin gene family expressed predominantly in muscle. J Biol Chem. 271(4):2255-2261.
106. Way, M., R. G. Parton. 1995. M-caveolin, a muscle-specific caveolin-related protein. FEBS Lett. 376(1-2):108-112.
107. Williams, T. M., M. P. Lisanti. 2004. The caveolin proteins. Genome Biol. 5(3):214.
108. Scherer, P. E., M. P. Lisanti, G. Baldini, M. Sargiacomo, C. C. Mastick, H. F. Lodish. 1994. Induction of caveolin during adipogenesis and association of GLUT4 with caveolin-rich vesicles. J Cell Biol. 127(5):1233-1243.
109. Monier, S., R. G. Parton, F. Vogel, J. Behlke, A. Henske, T. V. Kurzchalia. 1995. VIP21-caveolin, a membrane protein constituent of the caveolar coat, oligomerizes in vivo and in vitro. Mol Biol Cell. 6(7):911-927.
110. Scherer, P. E., R. Y. Lewis, D. Volonte, J. A. Engelman, F. Galbiati, J. Couet, D. S. Kohtz, E. van Donselaar, P. Peters, M. P. Lisanti. 1997. Cell-type and tissue-specific expression of caveolin-2. Caveolins 1 and 2 co-localize and form a stable hetero-oligomeric complex in vivo. J Biol Chem. 272(46):29337-29346.
111. Razani, B., S. E. Woodman, M. P. Lisanti. 2002. Caveolae: from cell biology to animal physiology. Pharmacol Rev. 54(3):431-467.
112. Lisanti, M. P., P. E. Scherer, J. Vidugiriene, Z. Tang, A. Hermanowski-Vosatka, Y. H. Tu, R. F. Cook, M. Sargiacomo. 1994. Characterization of caveolin-rich membrane domains isolated from an endothelial-rich source: implications for human disease. J Cell Biol. 126(1):111-126.
113. Sargiacomo, M., M. Sudol, Z. Tang, M. P. Lisanti. 1993. Signal transducing molecules and glycosyl-phosphatidylinositol-linked proteins form a caveolin-rich insoluble complex in MDCK cells. J Cell Biol. 122(4):789-807.
114. Lisanti, M. P., P. E. Scherer, Z. Tang, M. Sargiacomo. 1994. Caveolae, caveolin and caveolin-rich membrane domains: a signalling hypothesis. Trends Cell Biol. 4(7):231-235.
115. Ostrom, R. S., C. Gregorian, R. M. Drenan, Y. Xiang, J. W. Regan, P. A. Insel. 2001. Receptor number and caveolar co-localization determine receptor coupling efficiency to adenylyl cyclase. J Biol Chem. 276(45):42063-42069.
116. Ostrom, R. S., J. D. Violin, S. Coleman, P. A. Insel. 2000. Selective enhancement of beta-adrenergic receptor signaling by overexpression of adenylyl cyclase type 6: colocalization of receptor and adenylyl cyclase in caveolae of cardiac myocytes. Mol Pharmacol. 57(5):1075-1079.
117. Rybin, V. O., X. Xu, M. P. Lisanti, S. F. Steinberg. 2000. Differential targeting of beta -adrenergic receptor subtypes and adenylyl cyclase to cardiomyocyte caveolae. A mechanism to functionally regulate the cAMP signaling pathway. J Biol Chem. 275(52):41447-41457.
118. Schwencke, C., S. Okumura, M. Yamamoto, Y. J. Geng, Y. Ishikawa. 1999. Colocalization of beta-adrenergic receptors and caveolin within the plasma membrane. J Cell Biochem. 75(1):64-72.
119. Head, B. P., H. H. Patel, D. M. Roth, N. C. Lai, I. R. Niesman, M. G. Farquhar, P. A. Insel. 2005. G-protein-coupled receptor signaling components localize in both sarcolemmal

and intracellular caveolin-3-associated microdomains in adult cardiac myocytes. J Biol Chem. 280(35):31036-31044.
120. Garcia-Cardena, G., P. Martasek, B. S. Masters, P. M. Skidd, J. Couet, S. Li, M. P. Lisanti, W. C. Sessa. 1997. Dissecting the interaction between nitric oxide synthase (NOS) and caveolin. Functional significance of the nos caveolin binding domain in vivo. J Biol Chem. 272(41):25437-25440.
121. Michel, J. B., O. Feron, D. Sacks, T. Michel. 1997. Reciprocal regulation of endothelial nitric-oxide synthase by Ca2+-calmodulin and caveolin. J Biol Chem. 272(25):15583-15586.
122. Michel, J. B., O. Feron, K. Sase, P. Prabhakar, T. Michel. 1997. Caveolin versus calmodulin. Counterbalancing allosteric modulators of endothelial nitric oxide synthase. J Biol Chem. 272(41):25907-25912.
123. Schnitzer, J. E. 2001. Caveolae: from basic trafficking mechanisms to targeting transcytosis for tissue-specific drug and gene delivery in vivo. Adv Drug Deliv Rev. 49(3):265-280.
124. Conrad, P. A., E. J. Smart, Y. S. Ying, R. G. Anderson, G. S. Bloom. 1995. Caveolin cycles between plasma membrane caveolae and the Golgi complex by microtubule-dependent and microtubule-independent steps. J Cell Biol. 131(6 Pt 1):1421-1433.
125. Parton, R. G., B. Joggerst, K. Simons. 1994. Regulated internalization of caveolae. J Cell Biol. 127(5):1199-1215.
126. Montesano, R., J. Roth, A. Robert, L. Orci. 1982. Non-coated membrane invaginations are involved in binding and internalization of cholera and tetanus toxins. Nature. 296(5858):651-653.
127. Anderson, H. A., Y. Chen, L. C. Norkin. 1996. Bound simian virus 40 translocates to caveolin-enriched membrane domains, and its entry is inhibited by drugs that selectively disrupt caveolae. Mol Biol Cell. 7(11):1825-1834.
128. Shin, J. S., Z. Gao, S. N. Abraham. 2000. Involvement of cellular caveolae in bacterial entry into mast cells. Science. 289(5480):785-788.
129. Stang, E., J. Kartenbeck, R. G. Parton. 1997. Major histocompatibility complex class I molecules mediate association of SV40 with caveolae. Mol Biol Cell. 8(1):47-57.
130. Anderson, R. G., B. A. Kamen, K. G. Rothberg, S. W. Lacey. 1992. Potocytosis: sequestration and transport of small molecules by caveolae. Science. 255(5043):410-411.
131. Kamen, B. A., A. K. Smith, R. G. Anderson. 1991. The folate receptor works in tandem with a probenecid-sensitive carrier in MA104 cells in vitro. J Clin Invest. 87(4):1442-1449.
132. Glenney, J. R., Jr. 1989. Tyrosine phosphorylation of a 22-kDa protein is correlated with transformation by Rous sarcoma virus. J Biol Chem. 264(34):20163-20166.
133. Engelman, J. A., R. J. Lee, A. Karnezis, D. J. Bearss, M. Webster, P. Siegel, W. J. Muller, J. J. Windle, R. G. Pestell, M. P. Lisanti. 1998. Reciprocal regulation of neu tyrosine kinase activity and caveolin-1 protein expression in vitro and in vivo. Implications for human breast cancer. J Biol Chem. 273(32):20448-20455.
134. Koleske, A. J., D. Baltimore, M. P. Lisanti. 1995. Reduction of caveolin and caveolae in oncogenically transformed cells. Proc Natl Acad Sci U S A. 92(5):1381-1385.
135. Park, D. S., B. Razani, A. Lasorella, N. Schreiber-Agus, R. G. Pestell, A. Iavarone, M. P. Lisanti. 2001. Evidence that Myc isoforms transcriptionally repress caveolin-1 gene expression via an INR-dependent mechanism. Biochemistry. 40(11):3354-3362.
136. Razani, B., Y. Altschuler, L. Zhu, R. G. Pestell, K. E. Mostov, M. P. Lisanti. 2000. Caveolin-1 expression is down-regulated in cells transformed by the human papilloma virus

in a p53-dependent manner. Replacement of caveolin-1 expression suppresses HPV-mediated cell transformation. Biochemistry. 39(45):13916-13924.
137. Timme, T. L., A. Goltsov, S. Tahir, L. Li, J. Wang, C. Ren, R. N. Johnston, T. C. Thompson. 2000. Caveolin-1 is regulated by c-myc and suppresses c-myc-induced apoptosis. Oncogene. 19(29):3256-3265.
138. Liu, P., Y. Ying, Y. G. Ko, R. G. Anderson. 1996. Localization of platelet-derived growth factor-stimulated phosphorylation cascade to caveolae. J Biol Chem. 271(17):10299-10303.
139. Yamamoto, M., Y. Toya, R. A. Jensen, Y. Ishikawa. 1999. Caveolin is an inhibitor of platelet-derived growth factor receptor signaling. Exp Cell Res. 247(2):380-388.
140. Zundel, W., L. M. Swiersz, A. Giaccia. 2000. Caveolin 1-mediated regulation of receptor tyrosine kinase-associated phosphatidylinositol 3-kinase activity by ceramide. Mol Cell Biol. 20(5):1507-1514.
141. Galbiati, F., D. Volonte, J. A. Engelman, G. Watanabe, R. Burk, R. G. Pestell, M. P. Lisanti. 1998. Targeted downregulation of caveolin-1 is sufficient to drive cell transformation and hyperactivate the p42/44 MAP kinase cascade. Embo J. 17(22):6633-6648.
142. Scheel, J., J. Srinivasan, U. Honnert, A. Henske, T. V. Kurzchalia. 1999. Involvement of caveolin-1 in meiotic cell-cycle progression in Caenorhabditis elegans. Nat Cell Biol. 1(2):127-129.
143. Zenklusen, J. C., I. Bieche, R. Lidereau, C. J. Conti. 1994. (C-A)n microsatellite repeat D7S522 is the most commonly deleted region in human primary breast cancer. Proc Natl Acad Sci U S A. 91(25):12155-12158.
144. Jenkins, R., S. Takahashi, K. DeLacey, E. Bergstralh, M. Lieber. 1998. Prognostic significance of allelic imbalance of chromosome arms 7q, 8p, 16q, and 18q in stage T3N0M0 prostate cancer. Genes Chromosomes Cancer. 21(2):131-143.
145. Kerr, J., J. A. Leary, T. Hurst, Y. C. Shih, T. M. Antalis, M. Friedlander, E. Crawford, S. K. Khoo, B. Ward, G. Chenevix-Trench. 1996. Allelic loss on chromosome 7q in ovarian adenocarcinomas: two critical regions and a rearrangement of the PLANH1 locus. Oncogene. 13(8):1815-1818.
146. Zenklusen, J. C., J. C. Thompson, A. J. Klein-Szanto, C. J. Conti. 1995. Frequent loss of heterozygosity in human primary squamous cell and colon carcinomas at 7q31.1: evidence for a broad range tumor suppressor gene. Cancer Res. 55(6):1347-1350.
147. Hayashi, K., S. Matsuda, K. Machida, T. Yamamoto, Y. Fukuda, Y. Nimura, T. Hayakawa, M. Hamaguchi. 2001. Invasion activating caveolin-1 mutation in human scirrhous breast cancers. Cancer Res. 61(6):2361-2364.
148. Simons, K., E. Ikonen. 2000. How cells handle cholesterol. Science. 290(5497):1721-1726.
149. Smart, E. J., Y. Ying, W. C. Donzell, R. G. Anderson. 1996. A role for caveolin in transport of cholesterol from endoplasmic reticulum to plasma membrane. J Biol Chem. 271(46):29427-29435.
150. Li, S., K. S. Song, M. P. Lisanti. 1996. Expression and characterization of recombinant caveolin. Purification by polyhistidine tagging and cholesterol-dependent incorporation into defined lipid membranes. J Biol Chem. 271(1):568-573.

151. Murata, M., J. Peranen, R. Schreiner, F. Wieland, T. V. Kurzchalia, K. Simons. 1995. VIP21/caveolin is a cholesterol-binding protein. Proc Natl Acad Sci U S A. 92(22):10339-10343.
152. Fielding, C. J., A. Bist, P. E. Fielding. 1997. Caveolin mRNA levels are up-regulated by free cholesterol and down-regulated by oxysterols in fibroblast monolayers. Proc Natl Acad Sci U S A. 94(8):3753-3758.
153. Fielding, P. E., C. J. Fielding. 1995. Plasma membrane caveolae mediate the efflux of cellular free cholesterol. Biochemistry. 34(44):14288-14292.
154. Babitt, J., B. Trigatti, A. Rigotti, E. J. Smart, R. G. Anderson, S. Xu, M. Krieger. 1997. Murine SR-BI, a high density lipoprotein receptor that mediates selective lipid uptake, is N-glycosylated and fatty acylated and colocalizes with plasma membrane caveolae. J Biol Chem. 272(20):13242-13249.
155. de la Llera-Moya, M., G. H. Rothblat, M. A. Connelly, G. Kellner-Weibel, S. W. Sakr, M. C. Phillips, D. L. Williams. 1999. Scavenger receptor BI (SR-BI) mediates free cholesterol flux independently of HDL tethering to the cell surface. J Lipid Res. 40(3):575-580.
156. Graf, G. A., P. M. Connell, D. R. van der Westhuyzen, E. J. Smart. 1999. The class B, type I scavenger receptor promotes the selective uptake of high density lipoprotein cholesterol ethers into caveolae. J Biol Chem. 274(17):12043-12048.
157. Ji, Y., B. Jian, N. Wang, Y. Sun, M. L. Moya, M. C. Phillips, G. H. Rothblat, J. B. Swaney, A. R. Tall. 1997. Scavenger receptor BI promotes high density lipoprotein-mediated cellular cholesterol efflux. J Biol Chem. 272(34):20982-20985.
158. Daniel, E. E., J. Jury, Y. F. Wang. 2001. nNOS in canine lower esophageal sphincter: colocalized with Cav-1 and Ca2+-handling proteins? Am J Physiol Gastrointest Liver Physiol. 281(4):G1101-1114.
159. Darby, P. J., C. Y. Kwan, E. E. Daniel. 2000. Caveolae from canine airway smooth muscle contain the necessary components for a role in Ca(2+) handling. Am J Physiol Lung Cell Mol Physiol. 279(6):L1226-1235.
160. Martens, J. R., N. Sakamoto, S. A. Sullivan, T. D. Grobaski, M. M. Tamkun. 2001. Isoform-specific localization of voltage-gated K+ channels to distinct lipid raft populations. Targeting of Kv1.5 to caveolae. J Biol Chem. 276(11):8409-8414.
161. Yarbrough, T. L., T. Lu, H. C. Lee, E. F. Shibata. 2002. Localization of cardiac sodium channels in caveolin-rich membrane domains: regulation of sodium current amplitude. Circ Res. 90(4):443-449.
162. Scriven, D. R., A. Klimek, P. Asghari, K. Bellve, E. D. Moore. 2005. Caveolin-3 is adjacent to a group of extradyadic ryanodine receptors. Biophys J. 89(3):1893-1901.
163. Calaghan, S., E. White. 2006. Caveolae modulate excitation-contraction coupling and beta2-adrenergic signalling in adult rat ventricular myocytes. Cardiovasc Res. 69(4):816-824.
164. Lohn, M., M. Furstenau, V. Sagach, M. Elger, W. Schulze, F. C. Luft, H. Haller, M. Gollasch. 2000. Ignition of calcium sparks in arterial and cardiac muscle through caveolae. Circ Res. 87(11):1034-1039.
165. Ishikawa, H. 1968. Formation of elaborate networks of T-system tubules in cultured skeletal muscle with special reference to the T-system formation. J Cell Biol. 38(1):51-66.
166. Minetti, C., F. Sotgia, C. Bruno, P. Scartezzini, P. Broda, M. Bado, E. Masetti, M. Mazzocco, A. Egeo, M. A. Donati and others. 1998. Mutations in the caveolin-3 gene cause autosomal dominant limb-girdle muscular dystrophy. Nat Genet. 18(4):365-368.

167. Minetti, C., M. Bado, P. Broda, F. Sotgia, C. Bruno, F. Galbiati, D. Volonte, G. Lucania, A. Pavan, E. Bonilla and others. 2002. Impairment of caveolae formation and T-system disorganization in human muscular dystrophy with caveolin-3 deficiency. Am J Pathol. 160(1):265-270.
168. Galbiati, F., J. A. Engelman, D. Volonte, X. L. Zhang, C. Minetti, M. Li, H. Hou, Jr., B. Kneitz, W. Edelmann, M. P. Lisanti. 2001. Caveolin-3 null mice show a loss of caveolae, changes in the microdomain distribution of the dystrophin-glycoprotein complex, and T-tubule abnormalities. J Biol Chem. 276(24):21425-21433.
169. Woodman, S. E., D. S. Park, A. W. Cohen, M. W. Cheung, M. Chandra, J. Shirani, B. Tang, L. A. Jelicks, R. N. Kitsis, G. J. Christ and others. 2002. Caveolin-3 knock-out mice develop a progressive cardiomyopathy and show hyperactivation of the p42/44 MAPK cascade. J Biol Chem. 277(41):38988-38997.
170. Artman, M., H. Ichikawa, M. Avkiran, W. A. Coetzee. 1995. Na+/Ca2+ exchange current density in cardiac myocytes from rabbits and guinea pigs during postnatal development. Am J Physiol. 268(4 Pt 2):H1714-1722.
171. Levin, K. R., E. Page. 1980. Quantitative studies on plasmalemmal folds and caveolae of rabbit ventricular myocardial cells. Circ Res. 46(2):244-255.
172. Ratajczak, P., T. Damy, C. Heymes, P. Oliviero, F. Marotte, E. Robidel, R. Sercombe, J. Boczkowski, L. Rappaport, J. L. Samuel. 2003. Caveolin-1 and -3 dissociations from caveolae to cytosol in the heart during aging and after myocardial infarction in rat. Cardiovasc Res. 57(2):358-369.
173. Rybin, V. O., P. W. Grabham, H. Elouardighi, S. F. Steinberg. 2003. Caveolae-associated proteins in cardiomyocytes: caveolin-2 expression and interactions with caveolin-3. Am J Physiol Heart Circ Physiol. 285(1):H325-332.
174. Balijepalli, R. C., J. D. Foell, D. D. Hall, J. W. Hell, T. J. Kamp. 2006. Localization of cardiac L-type Ca^{2+} channels to a caveolar macromolecular signaling complex is required for β_2-adrenergic regulation. Proc Natl Acad Sci U S A. 103(19):7500-7505.
175. Bossuyt, J., B. E. Taylor, M. James-Kracke, C. C. Hale. 2002. Evidence for cardiac sodium-calcium exchanger association with caveolin-3. FEBS Lett. 511(1-3):113-117.
176. Foster, L. J., C. L. De Hoog, M. Mann. 2003. Unbiased quantitative proteomics of lipid rafts reveals high specificity for signaling factors. Proc Natl Acad Sci U S A. 100(10):5813-5818.
177. Cavalli, A., M. Eghbali, T. Y. Minosyan, E. Stefani, K. D. Philipson. 2007. Localization of sarcolemmal proteins to lipid rafts in the myocardium. Cell Calcium.
178. Chen-Izu, Y., S. L. McCulle, C. W. Ward, C. Soeller, B. M. Allen, C. Rabang, M. B. Cannell, C. W. Balke, L. T. Izu. 2006. Three-dimensional distribution of ryanodine receptor clusters in cardiac myocytes. Biophys J. 91(1):1-13.
179. Dan, P., E. Lin, J. Huang, P. Biln, G. Tibbits. 2007. Three dimensional distribution of cardiac Na^{+}- Ca^{2+} exchanger and ryanodine receptor during development. Biophys J. In press.
180. Cunha, S. R., N. Bhasin, P. J. Mohler. 2007. Targeting and stability of Na/Ca exchanger 1 in cardiomyocytes requires direct interaction with the membrane adaptor ankyrin B. J Biol Chem. 282(7):4875-4883.
181. Mohler, P. J., J. J. Schott, A. O. Gramolini, K. W. Dilly, S. Guatimosim, W. H. duBell, L. S. Song, K. Haurogne, F. Kyndt, M. E. Ali and others. 2003. Ankyrin-B mutation causes type 4 long-QT cardiac arrhythmia and sudden cardiac death. Nature. 421(6923):634-639.

182. Chauhan, V. S., S. Tuvia, M. Buhusi, V. Bennett, A. O. Grant. 2000. Abnormal cardiac Na^+ channel properties and QT heart rate adaptation in neonatal ankyrin B knockout mice. Circ Res. 86(4):441-447.
183. Mohler, P. J., A. O. Gramolini, V. Bennett. 2002. The ankyrin-B C-terminal domain determines activity of ankyrin-B/G chimeras in rescue of abnormal inositol 1,4,5-trisphosphate and ryanodine receptor distribution in ankyrin-B (-/-) neonatal cardiomyocytes. J Biol Chem. 277(12):10599-10607.
184. Goel, M., C. D. Zuo, W. G. Sinkins, W. P. Schilling. 2007. TRPC3 channels colocalize with Na^+-Ca^{2+} exchanger and Na+ pump in axial component of transverse-axial tubular system of rat ventricle. Am J Physiol Heart Circ Physiol. 292(2):H874-883.
185. Huang, J., C. van Breemen, K. H. Kuo, L. Hove-Madsen, G. F. Tibbits. 2006. Store-operated Ca^{2+} entry modulates sarcoplasmic reticulum Ca^{2+} loading in neonatal rabbit cardiac ventricular myocytes. Am J Physiol Cell Physiol. 290(6):C1572-1582.
186. Lachmanovich, E., D. E. Shvartsman, Y. Malka, C. Botvin, Y. I. Henis, A. M. Weiss. 2003. Co-localization analysis of complex formation among membrane proteins by computerized fluorescence microscopy: application to immunofluorescence co-patching studies. J Microsc. 212(Pt 2):122-131.
187. McDonald, R. L., J. Colyer, S. M. Harrison. 2000. Quantitative analysis of Na+-Ca2+ exchanger expression in guinea-pig heart. Eur J Biochem. 267(16):5142-5148.
188. Song, K. S., P. E. Scherer, Z. Tang, T. Okamoto, S. Li, M. Chafel, C. Chu, D. S. Kohtz, M. P. Lisanti. 1996. Expression of caveolin-3 in skeletal, cardiac, and smooth muscle cells. Caveolin-3 is a component of the sarcolemma and co-fractionates with dystrophin and dystrophin-associated glycoproteins. J Biol Chem. 271(25):15160-15165.
189. Sedarat, F., E. Lin, E. D. Moore, G. F. Tibbits. 2004. Deconvolution of confocal images of dihydropyridine and ryanodine receptors in developing cardiomyocytes. J Appl Physiol. 97(3):1098-1103.
190. Swedlow, J. R., K. Hu, P. D. Andrews, D. S. Roos, J. M. Murray. 2002. Measuring tubulin content in Toxoplasma gondii: a comparison of laser-scanning confocal and wide-field fluorescence microscopy. Proc Natl Acad Sci U S A. 99(4):2014-2019.